nature communications

Article

https://doi.org/10.1038/s41467-024-52600-2

USF2 and TFEB compete in regulating lysosomal and autophagy genes

Received: 15 February 2024

Accepted: 15 September 2024

Published online: 27 September 2024

Check for updates

Jaebeom Kim[1,14], Young Suk Yu[1,14], Yehwa Choi[1], Do Hui Lee[1], Soobin Han[1], Junhee Kwon[2], Taichi Noda[3,4,5], Masahito Ikawa[3,6], Dongha Kim[7], Hyunkyung Kim[8,9], Andrea Ballabio[10,11,12,13], Keun Il Kim[2] ✉ & Sung Hee Baek[1] ✉

Autophagy, a highly conserved self-digestion process crucial for cellular homeostasis, is triggered by various environmental signals, including nutrient scarcity. The regulation of lysosomal and autophagy-related processes is pivotal to maintaining cellular homeostasis and basal metabolism. The consequences of disrupting or diminishing lysosomal and autophagy systems have been investigated; however, information on the implications of hyperactivating lysosomal and autophagy genes on homeostasis is limited. Here, we present a mechanism of transcriptional repression involving upstream stimulatory factor 2 (USF2), which inhibits lysosomal and autophagy genes under nutrient-rich conditions. We find that USF2, together with HDAC1, binds to the CLEAR motif within lysosomal genes, thereby diminishing histone H3K27 acetylation, restricting chromatin accessibility, and downregulating lysosomal gene expression. Under starvation, USF2 competes with transcription factor EB (TFEB), a master transcriptional activator of lysosomal and autophagy genes, to bind to target gene promoters in a phosphorylation-dependent manner. The GSK3β-mediated phosphorylation of the USF2 S155 site governs USF2 DNA-binding activity, which is involved in lysosomal gene repression. These findings have potential applications in the treatment of protein aggregation-associated diseases, including α1-antitrypsin deficiency. Notably, USF2 repression is a promising therapeutic strategy for lysosomal and autophagy-related diseases.

Macroautophagy, referred to as 'autophagy', is a highly conserved self-digestion process pivotal for cellular homeostasis. While occurring moderately under basal conditions, this process is activated in response to environmental signals, notably nutrient starvation[1,2]. Autophagy begins with the sequestration of cytoplasmic materials into an expanding membrane known as the phagophore, which subsequently matures into a double-membrane vesicle, the autophagosome[1,2]. The fusion of autophagosomes with lysosomes forms autolysosomes, where cytoplasmic components undergo degradation. Lysosomal biogenesis and function are thus integral to the autophagic process, playing a crucial role in the degradation and recycling of long-lived proteins, carbohydrates, lipids, and nucleic acids. As indispensable components for cellular homeostasis and survival, lysosomes house over 60 hydrolytic enzymes and various cellular regulators[3]. Consequently, in humans, lysosomal dysfunction is associated with lysosomal storage disorders characterized by the aggregation of undigested cargo within lysosomes, leading to cellular dysfunction and tissue damage[4,5].

While the regulation of autophagy- and lysosome-based degradation in the cytoplasm has received considerable attention, the nuclear events, where the mechanism for the transcriptional activation

A full list of affiliations appears at the end of the paper. ✉e-mail: kikim@sookmyung.ac.kr; sbaek@snu.ac.kr

https://doi.org/10.1038/s41467-024-52600-2

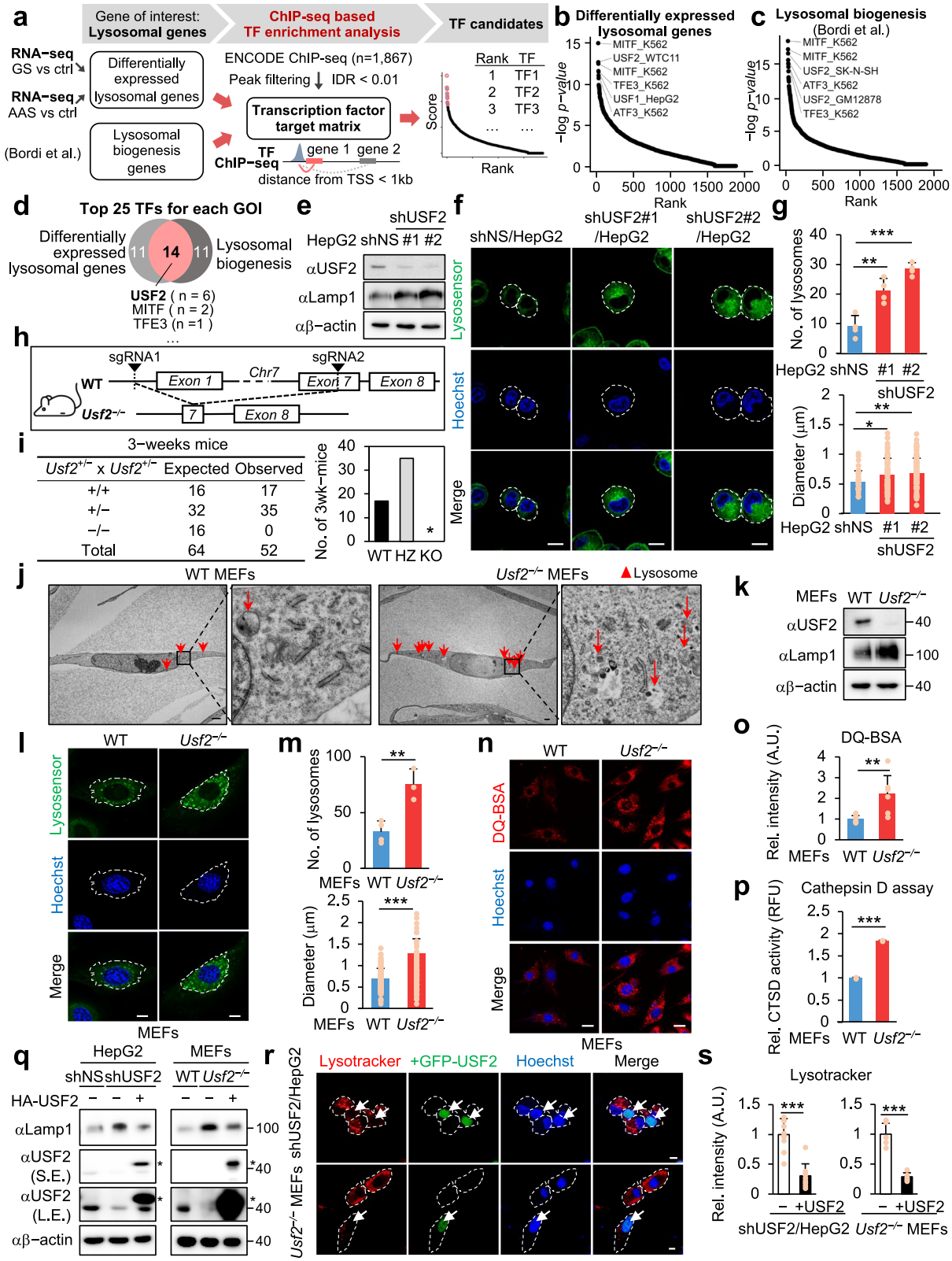

of autophagy and lysosomal genes have been largely studied, remain to be further explored. MiT/TFE family of transcription factors including the master regulator transcription factor EB (TFEB) facilitate autophagy and lysosomal function by up-regulating the transcription of relevant genes[6,7]. Forkhead box class O (FOXO) family proteins can also regulate autophagy in specific contexts[8,9]. Conversely, c-MYC inhibits autophagy and lysosome biogenesis by repressing the expression of MiT/TFE and FOXH1, along with the transcription of autophagy and lysosomal genes[10].

Epigenetic control, specifically histone modification, plays a pivotal role in regulating autophagic flux by altering chromatin structure[11]. We previously identified CARM1/PRMT4 as a critical coactivator of TFEB in autophagy[12]. Glucose deprivation activates the AMPK–SKP2–CARM1 signaling cascade, stabilizing CARM1 in the

Fig. 1 | USF2 represses the biogenesis of functionally mature lysosomes. a A schematic that illustrates a screening process to identify lysosome-associated transcription factors and the corresponding transcription factor (TF) enrichment ranks from the ENCODE TF ChIP-seq database. **b** TF enrichment rank plot in differentially expressed genes. **c** TF enrichment rank plot in the term of lysosomal biogenesis **d** Venn diagram illustrating the overlapping enriched TFs related to lysosomes. **e** Immunoblot analysis of USF2 and Lamp1 expression in shNS HepG2 and shUSF2 HepG2 cell lines. **f** Representative images depict Lysosensor staining in shNS HepG2 and shUSF2 HepG2 cell lines. These images were captured using a confocal microscope under identical settings. The white guidelines indicate the cell boundaries. Lysosensor, green; Hoechst, blue. Scale bar, 20 μm. **g** Quantification of lysosomal number per cell and diameter per lysosome in shNS HepG2 and shUSF2 HepG2 cell lines. $n = 4$ biologically independent samples. Statistical analysis was performed using a two-tailed *t*-test. shUSF2 HepG2#1 and shUSF2 HepG2#2 cell lines were individually compared to shNS HepG2. **h** Schematic drawing of the generation of *Usf2* whole-body knockout mice. **i** Summary of genotyping results for the offspring of *Usf2* heterozygous crosses. "Expected" represents the theoretical number of offspring expected based on the Mendelian ratio for an analysis of similar size. The graph on the right represents the "Observed" in the table. **j** Representative TEM images of WT and *Usf2*$^{-/-}$ MEFs. Scale bar, 2 μm. High magnification of the boxed areas is shown on the right. Lysosomes (red arrows). **k** Immunoblot analysis of USF2 and Lamp1 expression in WT and *Usf2*$^{-/-}$ MEFs. **l** Representative confocal images of Lysosensor staining in WT and *Usf2*$^{-/-}$ MEFs. **m** Quantification of lysosomal number per cell and diameter per lysosome in WT and *Usf2*$^{-/-}$ MEFs. $n = 4$ biologically independent samples. Statistics by two-tailed *t*-test using WT and *Usf2*$^{-/-}$ MEFs as a comparison. **n** Representative confocal images of DQ-BSA staining. WT and *Usf2*$^{-/-}$ MEFs were treated with DQ-BSA. DQ-BSA, red; Hoechst, blue. Scale bar, 20 μm. **o** Quantification of DQ-BSA intensity per cell in WT and *Usf2*$^{-/-}$ MEFs. $n = 6$ biologically independent samples. Statistics by two-tailed *t*-test using WT and *Usf2*$^{-/-}$ MEFs as a comparison. **p** Analysis of the activity of lysosomal cathepsin D in WT and *Usf2*$^{-/-}$ MEFs. $n = 2$ biologically independent samples. Statistics by two-tailed *t*-test using WT and *Usf2*$^{-/-}$ MEFs as a comparison. **q** Immunoblot analysis of shNS, shUSF2, and USF2 (GFP-USF2) reconstituted shUSF2 HepG2 cell lines (left), and WT, *Usf2*$^{-/-}$, and USF2 reconstituted *Usf2*$^{-/-}$ MEFs (right). **r** Representative images of Lysotracker staining in shUSF2 HepG2 cell line and *Usf2*$^{-/-}$ MEFs reconstituted with GFP-USF2. Lysotracker, red; GFP, green; Hoechst, blue. Scale bar, 10 μm. **s** Quantification of Lysotracker intensity per cell in shUSF2 HepG2 cell line and in *Usf2*$^{-/-}$ MEFs. $n = 9$ biologically independent samples for HepG2 cells and $n = 5$ biologically independent samples for MEFs. Statistics by two-tailed *t*-test using shNS and shUSF2 HepG2 cell line or WT and *Usf2*$^{-/-}$ MEFs as each comparison. Data are presented as mean ± standard error of the mean (SEM). *, $p < 0.05$; **, $p < 0.01$; ***, $p < 0.001$. Source data are provided as a Source Data file.

nucleus. Subsequently, CARM1 binds to TFEB in the promoter region, elevating histone H3 arginine 17 di-methylation (H3R17me2) levels and facilitating the transcriptional activation of—autophagy and lysosomal genes[12]. Under glucose deprivation, CARM1 methylates Pontin, inducing the binding of methylated Pontin to FOXO3a. This complex recruits TIP60 histone acetyltransferase to the enhancer regions of autophagy and lysosomal genes, promoting their expression[13]. Notably, downregulation of the histone acetyltransferase hMOF (also known as KAT8 or MYST1) during autophagy induction reduces histone H4 lysine 16 acetylation (H4K16Ac), and inhibiting this reduction enhances cell death[14].

Upstream stimulatory factors (USFs), including USF1 and USF2, are members of the bHLH-ZIP transcription factors that recognize the 5′-CANNTG-3′ E-box core sequence[15]. USFs regulate the expression of genes involved in the cell cycle[16], immune response[17], fatty acid synthesis[18], insulin signaling[19], and UV-induced pigmentation in melanocytes[20,21]. USF1 is implicated in familial combined hyperlipidemia, a common atherogenic dyslipidemia characterized by familial segregation of elevated triglycerides and/or total cholesterol[22]. Conversely, USF2 regulates processes related to metabolism[21], iron homeostasis[23], fertility[24], and growth[25]. The embryonic lethality observed in *Usf1/Usf2* double-knockout (KO) mice highlights their critical role during embryogenesis[26]. However, there exists a gap in understanding the nuclear mechanisms governing the transcriptional regulation of autophagy and lysosomal genes.

To address this knowledge gap, we investigate the pivotal role of USF2 as a transcriptional repressor for genes associated with lysosomal and autophagic processes in conjunction with the NuRD complex. Since USF2 and TFEB oppositely regulate major lysosomal genes, we also aimed to elucidate the mechanisms that control their competitive relationship. Furthermore, we explored the regulation of USF2 recruitment to target promoters and found that GSK3β-mediated phosphorylation of USF2 enhances its DNA-binding activity and amplifies the repression of lysosomal genes. We believe that our findings provide insights into cellular homeostasis and potential therapeutic strategies for protein-aggregation-related diseases.

Results

USF2 represses lysosomal biogenesis and autophagy

We conducted chromatin immunoprecipitation sequencing (ChIP-seq)-based transcription factor (TF) enrichment analysis of various lysosomal genes to identify lysosome-associated TFs. Leveraging ENCODE ChIP-seq data, which includes 1867 TFs, we constructed a TF target matrix based on TF binding to promoter regions (Fig. 1a). We identified candidate TFs that bind specifically to the promoters of the genes of interest, which included lysosomal genes differentially expressed under nutrient-deficient conditions and lysosomal biogenesis genes (Fig. 1b, c; Supplementary Data 1). Notably, the USF2 was consistently identified as a top candidate, along with well-known MiT/TFE proteins, including Microphthalmia-associated transcription factor (MITF) and TFE3 (Fig. 1d).

To assess whether USF2 participates in lysosomal gene regulation, we generated USF2 knockdown HepG2 cell lines using shRNA and analyzed the expression of LAMP1, a lysosomal membrane component. Notably, USF2 knockdown led to up-regulated LAMP1 expression (Fig. 1e). Analysis using LysoSensor, a fluorescent dye that labels acidic organelles in living cells, revealed stronger fluorescence in USF2 knockdown HepG2 cells compared with wild-type (WT) counterpart (Fig. 1f). USF2 knockdown increased the number and size of lysosomes (Fig. 1g). These results suggest that USF2 is a negative regulator of genes involved in lysosomal biogenesis.

We generated *Usf2*$^{-/-}$ mice by deleting exons 1–7 to monitor USF2 function in vivo (Fig. 1h). Genotyping of three-week-old offspring from *Usf2* heterozygous mating revealed an expected Mendelian ratio of *Usf2* WT and heterozygous pups, whereas no homozygous *Usf2*-KO pups were obtained (Fig. 1i), indicating their embryonic lethality. Therefore, we generated WT and *Usf2*$^{-/-}$ mouse embryonic fibroblasts (MEFs) from 13.5-day-old embryos and investigated whether USF2 participates in lysosomal biogenesis. Transmission electron microscopy of these MEFs revealed that *Usf2* KO substantially increased the number of lysosomes (Fig. 1j), which were presumably functionally mature as they were loaded with cargo. We performed additional experiments to validate these findings. Consistent with the results for USF2 knockdown HepG2 cells, *Usf2*$^{-/-}$ MEFs exhibited elevated LAMP1 expression compared with that in WT MEFs (Fig. 1k). LysoSensor analysis revealed stronger fluorescence and increased number and size of lysosomes in *Usf2*$^{-/-}$ MEFs than in WT MEFs (Fig. 1l, m).

Subsequently, we monitored the protein-degrading activity of the lysosomes using DQ-BSA. The fluorescence intensity from the degradation products of DQ-BSA was two-fold higher in *Usf2*$^{-/-}$ MEFs than in WT MEFs (Fig. 1n, o). Based on in vitro cathepsin D activity assay, *Usf2*$^{-/-}$ MEFs exhibited approximately two-fold higher proteolytic potential than WT MEFs (Fig. 1p). The increased lysosomal biogenesis observed in *Usf2*-deficient cells was reversed upon reintroduction of USF2. USF2 restoration reduced LAMP1 expression in both *Usf2*$^{-/-}$ MEFs and USF2 knockdown HepG2 cells (Fig. 1q) and reduced the numbers of lysosomes to WT levels (Fig. 1r, s). These results indicate that USF2 transcriptionally represses lysosomal genes, functioning as a negative regulator of lysosomal biogenesis and function.

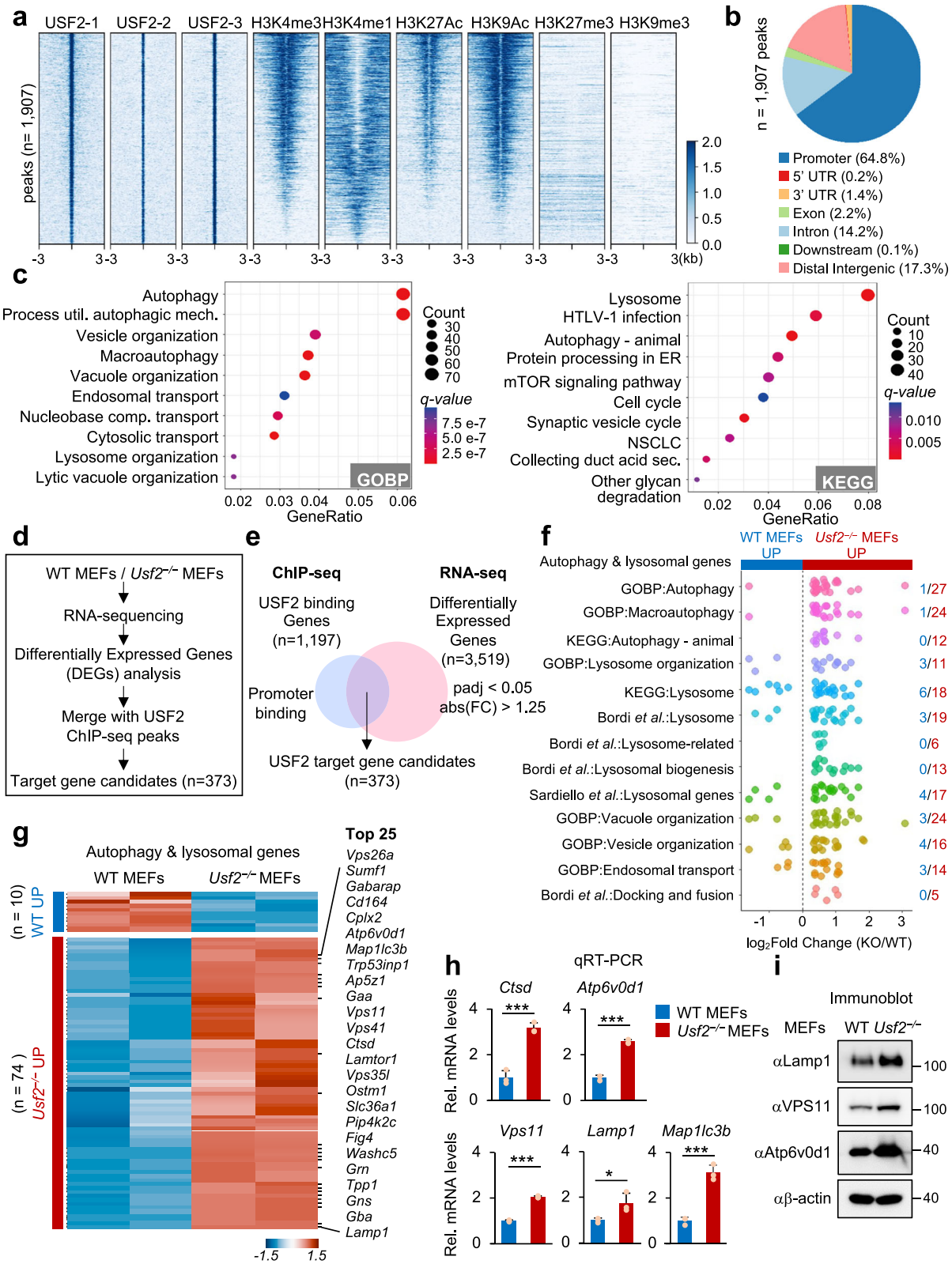

We also investigated whether USF2 affects autophagic activity. To assess autophagic flux, we used the lysosomal inhibitors including Bafilomycin A1 and Chloroquine. We found that Bafilomycin A1 and Chloroquine increase the autophagosome marker LC3-II level even in *Usf2*-deficient cells, and LC3-II levels were higher in *Usf2*$^{-/-}$ MEFs compared to WT cells (Supplementary Fig. 1a, b). LC3-puncta assay to determine the difference in autophagosome formation between WT and *Usf2*$^{-/-}$ MEFs also showed increased LC3 puncta in *Usf2*$^{-/-}$ MEFs compared to WT cells (Supplementary Fig. 1c, d). These findings reveal that USF2 represses not only lysosome biogenesis but also autophagosome formation.

USF2 transcriptionally represses lysosomal genes

To elucidate the mechanisms underlying USF2 function, we utilized mouse USF2 ENCODE ChIP-seq datasets, examining changes in histone markers in regions exhibiting repetitive peaks (Fig. 2a). Although

Fig. 2 | ChIP-sequencing and RNA-sequencing reveal that USF2-dependent genes are enriched in lysosomal genes. a Analysis of histone markers in regions with USF2 peaks. Each row indicates a 6 kb window centered on a USF2 binding site. **b** Annotation of USF2 peaks based on their genomic location. **c** Gene ontology and KEGG pathway analysis of USF2-bound genes. **d** Schematic illustrating the integrated analysis of RNA-seq results from WT and *Usf2*$^{-/-}$ MEFs and ChIP-seq results for USF2. **e** Venn diagram showing 373 USF2 target candidates obtained by combining USF2 binding genes from USF2 ChIP-seq and differentially expressed genes (DEGs) from RNA-seq. **f** Fold change distribution of genes belonging to autophagy and lysosomal gene lists based on the presence or absence of USF2. Blue numbers indicate the number of genes with increased expression in WT, while red numbers indicate the number of genes with increased expression in *Usf2*$^{-/-}$. **g** Heatmap of the gene expression of USF2 target genes belonging to autophagy and lysosomal genes. Top 25 significantly upregulated genes in *Usf2*$^{-/-}$ are listed on the right. **h** qRT-PCR assay of USF2 target genes in WT and *Usf2*$^{-/-}$ MEFs. $n = 3$ technical replicates. Statistics by two-tailed *t*-test using WT and *Usf2*$^{-/-}$ MEFs as a comparison. Data are presented as mean ± SEM. *, $p < 0.05$; ***, $p < 0.001$. **i** Immunoblot assay of USF2 target proteins in WT and *Usf2*$^{-/-}$ MEFs. Source data are provided as a Source Data file.

certain peaks revealed the presence of the enhancer-marker H3K4me1, most peaks demonstrated significant enrichment of the promoter marker H3K4me3. Consistent with this, 65 % of the USF2 peaks were located within promoter regions (Fig. 2b).

Gene ontology (GO) and Kyoto Encyclopedia of Genes and Genomes (KEGG) pathway analyses, using a gene set that USF2 binds to the promoter, revealed significant enrichment of autophagy- and lysosome-related terms, indicating the strong association between USF2-bound genes and these processes (Fig. 2c). RNA-seq analysis of *Usf2*$^{-/-}$ MEFs was conducted to assess USF2-mediated regulation of gene expression. Integration of the ChIP-seq and RNA-seq data revealed that 373 differentially expressed genes (DEGs) were regulated by direct USF2 binding (Fig. 2d, e). In USF2 target candidates categorized under autophagy and lysosome GO-terms, the genes increased in *Usf2*$^{-/-}$ MEFs outnumbered the decreased ones (Fig. 2f). Of the 84 autophagy- and lysosome-related genes, 74 were up-regulated in *Usf2*$^{-/-}$ MEFs compared with that in WT MEFs (Fig. 2g; Supplementary Data 2). Upregulation in *Usf2*$^{-/-}$ MEFs of lysosomal genes, including *Ctsd*, *Atp6v0d1*, *Lamp1*, *Vps11*, and *Map1lc3b* was confirmed using qRT-PCR (Fig. 2h) and immunoblotting (Fig. 2i). These results suggest USF2 binds directly to autophagy- and lysosome-related gene promoters and functions as a transcriptional repressor of these genes.

USF2 reduces chromatin accessibility

We examined whether USF2 represses target gene transcription by modulating chromatin accessibility. ATAC-seq analysis integrating ChIP-seq data revealed 2390 ATAC-seq peaks within a 2 kb window centered on the USF2 peak (Fig. 3a), mostly within promoter regions (Fig. 3b); 456 peaks exhibited significantly different chromatin accessibility in the presence or absence of USF2 (Fig. 3c). Among the differentially opened peaks (DOPs), most (353) exhibited enhanced chromatin opening in *Usf2*$^{-/-}$cells compared with that in WT cells, indicating that USF2 reduces chromatin accessibility (Fig. 3d; Supplementary Data 3). To investigate the association between USF2-mediated regulation of chromatin accessibility and gene expression, we conducted an integrated analysis by merging the RNA-seq data; this helped identify 173 DEG-related DOPs (Fig. 3e), most (154) in the promoter region of the DEGs (Fig. 3f). For the promoter-located DOPs, chromatin accessibility and mRNA expression were strongly correlated (Fig. 3f).

We next applied a multiomics approach to clarify the impact of USF2 binding on chromatin accessibility and gene expression. Integrating the USF2 ChIP-seq, RNA-seq, and ATAC-seq data revealed that, of the 154 ChIP-seq-identified genes exhibiting direct USF2 binding, 125 exhibited reduced chromatin accessibility in the region of direct binding; of these, 114 exhibited reduced mRNA expression (Fig. 3g). GO analysis of the genes with DOPs in their promoters revealed that many of the USF2-regulated genes were associated with autophagy and lysosomal processes (Fig. 3h). Among the 39 DOPs associated with autophagy and lysosomal genes, most (34) exhibited increased chromatin accessibility and gene expression under *Usf2*$^{-/-}$ condition compared with that in WT (Fig. 3i). Peak visualization revealed the regulatory dynamics of USF2-target genes, including *Lamp1, Ctsd, Atp6v0d1*, and *Gns* (Fig. 3j). These results indicate that USF2 binding participates in reducing chromatin accessibility, ultimately repressing autophagy and lysosomal gene expression.

USF2 exerts transcriptional repression through the NuRD complex

Based on the findings that USF2 limits the accessibility of chromatin for lysosomal and autophagy gene expression, we hypothesized that corepressor complexes are required for USF2-mediated transcriptional repression. We next identified the binding partners of USF2 via biochemical purification followed by LC-MS/MS (Fig. 4a; Supplementary Data 4). The nucleosome remodeling and deacetylation (NuRD) complex, which includes histone deacetylase (HDAC) 1 and 2, had the highest scores in terms of the $-\log_{10}$(false discovery rate) (Fig. 4b, c).

To investigate the co-recruitment of USF2 and NuRD complex to the target genomic regions, we examined the recruitment of the NuRD complex subunit (HDAC1, HDAC2, CHD4, GATAD2A, GATAD2B, and MTA1) to USF2-bound genomic regions using human ENCODE ChIP-seq data. Our analysis revealed substantial enrichment of the NuRD complex within the USF2-binding regions (Fig. 4d), supporting their co-recruitment and highlighting their potential collaboration in chromatin regulation. Co-immunoprecipitation assay results indicated that USF2 interacted with HDAC1 and 2, the core enzymes in NuRD complex having deacetylase function on H3K27Ac, and with other NuRD complex subunits including MTA1 (Fig. 4e and Supplementary Fig. 2a).

ChIP-seq analysis of *Usf2*$^{-/-}$ MEFs revealed higher H3K27Ac peaks in *Usf2*$^{-/-}$ MEFs compared with those in WT MEFs (Fig. 4f). The promoter regions of *Lamp1, Atp6v0d1*, and *Gns* exhibited higher H3K27Ac peaks in *Usf2*$^{-/-}$ MEFs compared with that in WT MEFs, likely owing to reduced deacetylation in the absence of USF2 (Fig. 4g). ChIP assay revealed co-recruitment of USF2 and HDAC1 to the promoter regions of autophagy and lysosomal genes, resulting in reduced H3K27Ac levels (Fig. 4h), confirming that NuRD mediates the repressive function of USF2.

We investigated whether an HDAC1 inhibitor can trigger lysosomal activation in line with the epigenetic repressive model of USF2. We found that Valproic acid (VPA), a known HDAC1 inhibitor, activated lysosomal and autophagy-related genes (Supplementary Fig. 2b). These results further confirm that USF2, in conjunction with the NuRD complex that includes HDAC1, collaboratively represses lysosomal and autophagic activity (Fig. 4i).

USF2 and TFEB competitively bind to lysosomal genes

In silico motif analysis revealed that most of the USF2-binding regions contain a 5′-GTCACGTG-3′ sequence that belongs to the E-box motif (Fig. 5a). TFE3 and MITF, which are well-known regulators of autophagy- and lysosome-related genes, were highly enriched, identifying them as potential TFs that bind to this motif (Fig. 5a). TFEB was not identified, as there was insufficient ENCODE data for TFEB. All MiT/TFE family members bind to the CLEAR motif[7,26].

Examination of human ChIP-seq data revealed that TFE3 and MITF bind to the same genomic regions as USF2 (Fig. 5b, c). Peak visualization indicated that TFE3 and MITF bound to USF2 target genes, including *Lamp1, Vps11, Atp6v0d1*, and *Gaa* (Fig. 5d). ChEA TF enrichment analysis, using up-regulated genes in *Usf2* KO (Fig. 5e;

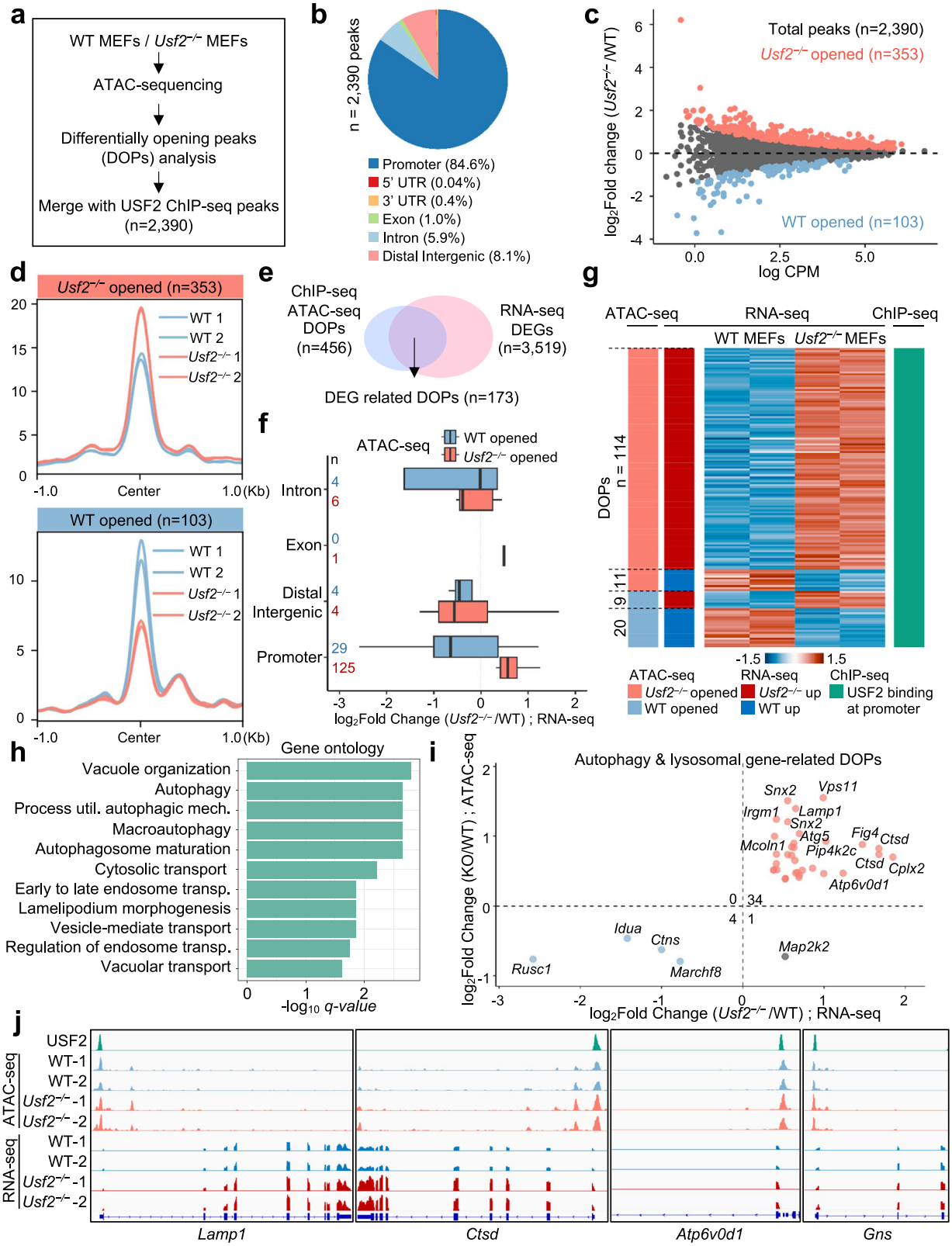

Supplementary Data 5), identified TFEB and MITF as the most enriched transcription factors for these genes (Fig. 5f). Perturbation analysis showed that the genes repressed by USF2 were most similar to those with increased expression upon TFEB overexpression (Fig. 5g). Collectively, we hypothesized that USF2 and MiT/TFE antagonistically regulate gene expression by competing for the same binding motifs.

We conducted immunoblotting analysis along with cell fractionation and immunocytochemistry using an anti-TFEB antibody to identify the subcellular localization of TFEB. As a result, no difference in the translocation of TFEB upon glucose starvation was observed between WT and *Usf2*$^{-/-}$ MEFs (Supplementary Fig. 3a–c). We investigated the recruitment of TFEB to the target gene promoters in *Usf2*$^{-/-}$

Fig. 3 | USF2 binding reduces chromatin accessibility and expression of autophagy and lysosomal genes. a Schematic of the ATAC-seq analysis workflow for WT and *Usf2*$^{-/-}$ MEFs. **b** Annotation of ATAC-seq peaks based on their genomic location. **c** A scatter plot illustrating ATAC-seq results shows peaks that are more accessible in *Usf2*$^{-/-}$ depicted in red, and those more accessible in WT depicted in blue. **d** Read density plots for DOPs that are more accessible in *Usf2*$^{-/-}$ (upper) and WT (bottom). **e** Venn diagram showing 173 DEG-related DOPs obtained by combining DOPs from USF2 ChIP-seq and ATAC-seq results and DEGs obtained from RNA-seq. **f** Box plot illustrating the expression changes of the nearest genes to DEG-related DOPs at each genomic location. The number on the left of the box plot represents the number of DEG-related DOP used in the graph. For box plots, the vertical line represents the median value, the lower and upper quartiles represent the 25th and 75th percentile, and the whiskers show the maximum and minimum values (excluding the outliers). **g** Heatmap illustrating the expression of genes closest to DEG-related DOPs. **h** Gene ontology analysis of the genes showing DOPs in the promoters. **i** Graph depicting the correlation between chromatin accessibility and gene expression in DOPs associated with autophagy and lysosomal genes. **j** Visualization of USF2 ChIP-seq peaks, ATAC-seq signals, and RNA-seq coverage plots in USF2 target genes.

cells during glucose starvation. The ChIP assay revealed that glucose starvation increased the recruitment of TFEB to the promoter in *Usf2*$^{-/-}$ cells as well (Supplementary Fig. 3d). Thus, our data indicate that USF2 does not affect the nuclear translocation of TFEB.

Although the major localization of TFEB at steady state is the cytoplasm, it is known that the localization of TFEB is dynamically regulated by the rate of nuclear export and import even at steady state[27]. Therefore, even under steady state condition TFEB is able to promote the expression of its target genes, which can be inhibited by USF2. We also verified that some TFEB is present in the nucleus even at a steady state (Supplementary Fig. 3a–c). We examined the impact of *Usf2* knockout on the recruitment of TFEB to the promoters of target genes under steady state condition. ChIP assays revealed an enhancer recruitment of TFEB in *Usf2* knockout cells compared to WT cells (Fig. 5h). Moreover, the knockdown of TFEB by siRNA in *Usf2* knockout or knockdown cells reduced the expression of autophagy and lysosomal genes (Fig. 5i and Supplementary Fig. 3e). Additionally, increased levels of H3K27Ac in *Usf2* knockout cells were reduced following TFEB knockdown (Supplementary Fig. 3f). The CLEAR sequence is also a binding site for TFE3 and MITF, homologs of TFEB, which have a cooperative and partially overlapping function, including the regulation of lysosomal biogenesis and autophagy. Therefore, the effect of TFEB knock-down is partial due to the compensatory effects of TFE3 and MITF. These data suggest that the upregulation of autophagy/lysosome gene expression by *Usf2* knockout is TFEB-dependent at steady state.

ChIP-seq was used to examine whether glucose starvation has a comparable impact on the occupancy of target gene promoters by USF2. Upon glucose starvation, the USF2 target genes all exhibited fewer USF2 ChIP peaks, indicating that USF2 remains bound to the promoters of its target genes in the presence of glucose and dissociates upon glucose starvation which is opposite to TFEB action (Fig. 5j). Using ChIP assays, we confirmed that USF2 recruitment to the promoter regions of *Atp6v0d1*, *Lamp1*, and *Ctsd* was reduced under glucose starvation and amino acid starvation (Supplementary Fig. 3g, h).

We further investigated whether TFEB and USF2 competitively bind to the same promoter region, using the *Lamp1* promoter-luciferase reporter containing the CLEAR motif. Introduction of TFEB alone up-regulated luciferase activity, whereas its co-transfection with USF2 inhibited this upregulation (Fig. 5k). Overexpression of the USF2 WT repressed TFEB-induced luciferase activity, whereas overexpression of the USF2 DNA-binding domain mutant failed to repress it (Fig. 5k), indicating that USF2–DNA binding is vital in competing with TFEB in transcriptional repression. ChIP assay revealed that glucose starvation reduced USF2 recruitment but increased that of TFEB to the *Lamp1* promoter region (Fig. 5l). Subsequently, to examine the role of USF2 under nuclear co-localization of TFEB and USF2, we performed RNA-seq under glucose or amino acid starvation. USF2-mediated gene repression was maintained even when TFEB was translocated into the nucleus, and in the absence of USF2, its target gene expression was hyperactivated during both glucose and amino acid starvation (Fig. 5m and Supplementary Fig. 3i, j; Supplementary Data 5).

USF2 recruitment to USF2 target gene promoter regions and their H3K27Ac levels were examined in *TFEB*-deficient cells. Under glucose starvation, TFEB depletion increased USF2 recruitment to lysosomal gene promoters and reduced their H3K27Ac levels (Fig. 5n). Therefore, in the absence of TFEB, USF2 binding to lysosomal gene promoters is increased, thus enhancing transcriptional repression. USF2 and TFEB, therefore, share certain lysosomal genes as common targets while antagonistically regulating their transcription (Fig. 5o).

USF2 phosphorylation increases its DNA-binding activity

USF2 phosphorylation modulates its DNA-binding activity[28,29]. In granulosa cells, protein kinase A phosphorylates USF2, increasing its binding to the E-box[29]. GSK3β phosphorylates USF2, enhancing its DNA binding[28]. Therefore, we examined the potential role of USF2 phosphorylation in lysosomal gene repression: under nutrient-rich conditions, USF2 was phosphorylated, and λ-phosphatase reduced its phosphorylation (Fig. 6a).

USF2 is phosphorylated at S155 and T230 by GSK3β and at S222 by CDK5 (Fig. 6b)[28,30]. To examine the functional significance of USF2 phosphorylation, we generated the S155A, S222A, and T230A mutants. USF2 phosphorylation was almost entirely abolished in the S155A mutant, whereas it was retained in the S222A and T230A mutants (Fig. 6c). To investigate the effects of USF2 S155 phosphorylation, we expressed the USF2 WT or the S155A mutant in *Usf2*$^{-/-}$ cells and compared their DNA-binding activity. The S155A mutant exhibited reduced DNA binding to lysosomal gene promoter regions (Fig. 6d). Target lysosomal gene mRNA and protein levels were repressed when the USF2 WT was expressed but not when the S155A mutant was expressed (Fig. 6e, f). Similarly, *Usf2* KO-mediated upregulation of lysosomal biogenesis was abolished when the WT, but not the S155A mutant, was expressed (Fig. 6g, h). In contrast to the S155A mutant, we generated the phospho-mimetic mutant S155E of USF2 to further explore the function of USF2 phosphorylation (Supplementary Fig. 4a). Upon glucose starvation, WT USF2 undergoes dephosphorylation, resulting in its dissociation from the promoter and an increase in TFEB recruitment. However, the S155E mutant retains the phospho-mimetic effect even during glucose starvation, reducing TFEB recruitment (Supplementary Fig. 4b). Consequently, even under glucose starvation, TFEB target genes are not activated due to the presence of the USF2 S155E mutant (Supplementary Fig. 4c). Taken together, these data suggest that USF2 antagonizes TFEB by binding to the CLEAR motif in phosphorylation-dependent manner, and that phosphorylation of USF2 at S155 further enhances this antagonism.

Treatment with LiCl, a GSK3β inhibitor, reduced USF2 phosphorylation at S155 (Fig. 6i) and reversed the GSK3β-mediated increase in USF2 phosphorylation (Fig. 6j). The ChIP assay revealed that LiCl treatment reduced USF2 binding to lysosomal gene promoter regions (Fig. 6k). Glucose starvation and amino acid starvation reduced USF2 phosphorylation while decreasing GSK3β activity[31,32] (Fig. 6l, m and Supplementary Fig. 4d, f). Immunostaining revealed that the phosphorylation of GSK3β at S9, which is its inactive form, was elevated during glucose or amino acid deprivation, suggesting an inhibition of GSK3β activity within the nucleus (Fig. 6n and Supplementary Fig. 4g). As a result, since GSK3β is crucial for the phosphorylation of USF2, its reduced activity under glucose or amino acid deprivation leads to a decrease in USF2 phosphorylation.

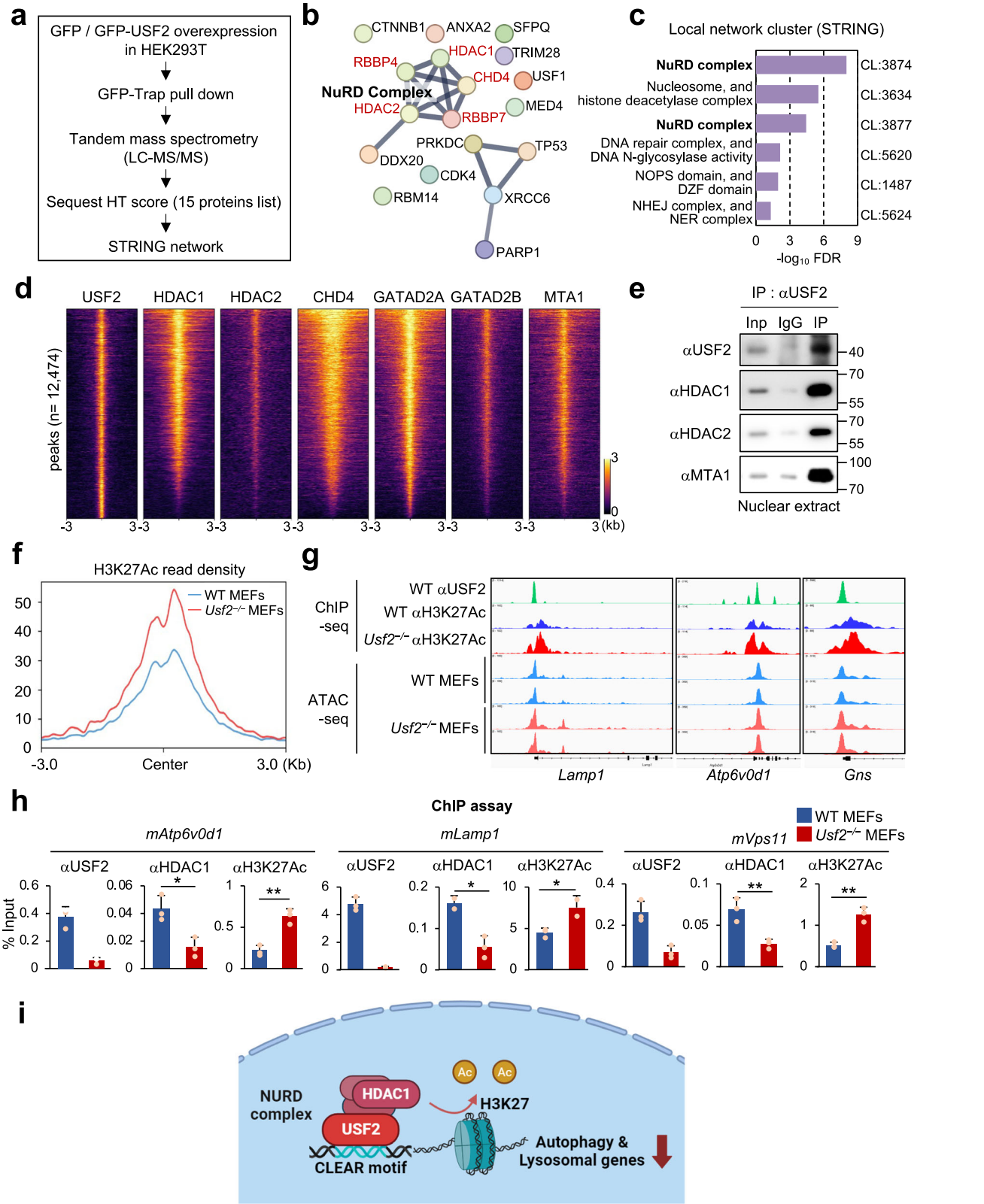

Inhibiting USF2 enhances α1-antitrypsin Z variant (ATZ) clearance

Subsequently, we investigated whether the elevated lysosome biogenesis in *Usf2*$^{-/-}$ cells could be recapitulated in *Usf2*$^{-/-}$ embryos. *Usf2*$^{-/-}$ mouse embryos exhibit increased Lamp1 expression overall, with a particularly dramatic increase observed in liver tissue, revealing that USF2 functions in lysosomal repression in the liver (Fig. 7a and Supplementary Fig. 5a).

We investigated whether USF2 deficiency-mediated enhancement of autophagy and lysosomal activity in the liver could be used to achieve clearance of misfolded protein aggregates. Therefore, we used the α1-antitrypsin (A1AT) Z variant (E342K; known as ATZ). α1-antitrypsin deficiency, the most prevalent inherited metabolic liver disease, involves misfolding and aggregation of ATZ within hepatocyte endoplasmic reticulum (ER) lumens[33]. Chronic accumulation of ATZ causes ER stress, leading to hepatocyte apoptosis, liver cirrhosis, and

Fig. 4 | USF2 represses lysosomal genes along with NuRD complex through H3K27 deacetylation. a Flowchart of the experiment to identify USF2-binding proteins. **b** Visualization of the binding network of USF2 binding partners obtained through LC-MS/MS using the STRING database. **c** Results of the local network cluster analysis in STRING using USF2 binding partners. **d** Heatmap depicting the enrichment of NURD complex components at USF2 binding sites. Each row indicates a 6 kb window centered on a USF2 binding site. **e** Binding between USF2 and NuRD complex subunits. Immunoprecipitation assay was performed by pulling down USF2, followed by immunoblotting with anti-HDAC1, anti-HDAC2, and anti-MTA1 antibodies to detect the endogenous protein expression levels. The representative images supported by the relevant statistics have been chosen from three independent preparations with similar outcomes. **f** Read density plots for ChIP-seq peaks of H3K27Ac in WT and *Usf2*$^{-/-}$ MEFs. **g** Visualization of USF2 and H3K27Ac ChIP-seq peaks, and ATAC-seq signals in USF2 target genes. **h** ChIP assays on USF2-dependent promoters in WT and *Usf2*$^{-/-}$ MEFs. $n = 3$ technical replicates. Statistics by two-tailed *t*-test using WT and *Usf2*$^{-/-}$ MEFs as a comparison. **i** Schematics of the repression mechanism of USF2-NuRD complex. Data are presented as mean ± SEM. *, $p < 0.05$; **, $p < 0.01$; ***, $p < 0.001$. Source data are provided as a Source Data file.

potentially hepatocellular carcinoma[34,35]. While the proteasome degrades soluble monomeric ATZ species via ER-associated protein degradation (ERAD), autophagy and lysosomes target the insoluble aggregated counterparts[33,36].

To examine whether USF2 participates in ATZ clearance via lysosomal activation, we generated GFP-ATZ-overexpressing HepG2 cells. USF2 knockdown using siRNA enhanced lysosomal activation, reduced GFP-ATZ protein levels (Fig. 7b), and decreased ATZ aggregation (Fig. 7c), without affecting GFP-ATZ mRNA expression (Supplementary Fig. 5b). USF2 knockdown reduced ATZ protein levels, which were largely restored by inhibiting lysosomal activity using BafA1 (Fig. 7d, e). USF2 knockdown, therefore, facilitates ATZ degradation via a lysosome-dependent pathway.

Immunocytochemistry was used to examine the effects of USF2 knockdown on lysosomal degradation of ATZ in GFP-ATZ cells treated with or without BafA1. LAMP1 staining was more intense in USF2 knockdown cells than in WT cells, regardless of BafA1 treatment, indicating increased lysosome biogenesis (Fig. 7f, g). In USF2 knockdown cells, ATZ staining intensity was low in the absence of BafA1 and was restored by BafA1 treatment. The strong LAMP1 and ATZ co-staining signal in BafA1-treated cells reflects lysosomal accumulation of ATZ (Fig. 7f, h).

We extended the observed reciprocal relationship between TFEB and USF2 to ATZ degradation. TFEB-overexpression-mediated lysosomal gene activation can facilitate ATZ aggregate degradation[37]. Under TFEB overexpression, USF2 knockdown further reduced GFP-ATZ levels (Fig. 7i, j), and ATZ aggregates (Fig. 7k, l). USF2 knockdown promoted ATZ degradation by enhancing autophagy and lysosomal biogenesis, providing a potential strategy for preventing the intracellular aggregation of ATZ. These findings suggest the combined use of TFEB activation and USF2 depletion as a therapeutic approach targeting lysosomal activation in protein aggregation-related disorders.

Discussion

Homeostatic regulation is critical in maintaining cellular viability and the basal metabolism for autophagy and lysosomal genes. TFEB and MiT/TFE enhance autophagy and lysosomal function by activating the transcription of relevant genes. The current findings reveal a transcriptional repression mechanism involving USF2 and validate its importance as a potent repressor of lysosomal and autophagic processes. There are several key findings. First, under nutrient-rich conditions, USF2 binds to the CLEAR motifs in lysosomal and autophagic gene promoters. Second, USF2 interacts with HDAC1, reducing both H3K27Ac levels and chromatin accessibility, effectively inhibiting lysosomal and autophagy-related gene expression and thus maintaining basal gene expression levels. Third, under nutrient starvation, USF2 competes with TFEB for binding to the CLEAR motif of lysosomal genes. Finally, GSK3β-mediated USF2 phosphorylation at S155 is crucial for regulating USF2 DNA-binding activity in repressing lysosomal genes. The repressive effects of USF2, along with competitive regulation by TFEB, hold great promise for addressing protein aggregation-related diseases, including α1-antitrypsin deficiency.

The transcriptional and epigenetic mechanisms up-regulating gene expression to promote autophagy and lysosomal biogenesis have been extensively studied. Nonetheless, our understanding of the processes involved in repressing gene expression to suppress autophagy and lysosomal function remains limited. The mechanism of action of USF2 differs from that of c-MYC, although it also represses autophagy and lysosomal biogenesis[10]. Interestingly, while c-MYC suppresses the expression of MiT/TEF proteins and FOXH1 and of lysosomal and autophagy-related genes, USF2 did not suppress TFEB expression. c-MYC represses expression by binding to HDAC1/2, primarily to HDAC2. Treatment with HDAC inhibitors induces upregulation of lysosomal biogenesis and MiT/TFE expression[10]. We examined the impact of the HDAC1 inhibitor, Valproic acid (VPA), on USF2 target genes. The qRT-PCR assay showed that VPA treatment activated autophagy and lysosomal genes (Supplementary Fig. 2b). This suggests that HDAC1 inhibitors can mimic USF2 depletion, leading to the activation of autophagy and lysosome-related genes.

Most studies on the relationship between USF2 and autophagy suggest that USF2 inhibits autophagy, but there are conflicting results. In MEFs, USF2 depletion elevated autophagy and increased the number and size of lysosomes[38], and in a cerebral ischemia-reperfusion injury model using HT22 neurons, USF2 depletion also increased autophagy and cell survival[39]. In addition, USF2 was reported to inhibit the expression of STX6 in hepatocellular carcinoma cells, where STX6 plays an important role in autophagosome-lysosome fusion[40]. Conversely, a recent study reported that USF2 enhances autophagy in chronic lymphocytic leukemia cells, thereby promoting leukemia progression[41]. Our comprehensive and detailed study of the regulation of autophagy and lysosome-related gene expression by USF2 concludes that USF2 acts as a repressor of these genes. However, since USF2 does not regulate the expression of all autophagy and lysosome-related genes, other possibilities cannot be ruled out.

Phosphorylation of TFE family proteins, including TFEB, regulates their translocation, and the mechanisms are well documented. TFEB and TFE3 are phosphorylated by mTORC1, which sequesters them in the cytoplasm. However, when autophagy is activated, they undergo dephosphorylation and translocate into the nucleus[42,43]. GSK3β phosphorylates TFEB (dependent on mTORC1 activation) at Ser138, promoting its nuclear export[27,44]. However, USF2 phosphorylation is not associated with translocation but with its DNA-binding activity. Phosphorylation of USF2 at Ser155 by GSK3 β enhances its DNA binding to the target promoters. Intriguingly, GSK3β-dependent phosphorylation enhances both USF2 DNA-binding (enhancing transcriptional repression) and cytoplasmic retention of TFEB (attenuating transcriptional activation). Therefore, under nutrient starvation, autophagy and lysosomal gene activation can be enhanced by reducing GSK3β activity and thereby enhancing TFEB dephosphorylation and nuclear translocation. However, dephosphorylation of USF2 does not appear to completely eliminate its DNA-binding ability, as reconstitution of the S155A mutant in *Usf2*$^{-/-}$ cells also suppressed lysosomal gene expression, albeit weaker than WT. Therefore, although USF2 phosphorylation regulates its DNA-binding activity, this may alter the competitive binding priority of various transcription factors, including TFEB, at lysosomal and autophagy-related gene promoters. Under physiological conditions, such regulation can prevent excessive activation of autophagy and lysosomes; however, when activation of autophagy and lysosomal processes is required, this is facilitated by impeding their repression.

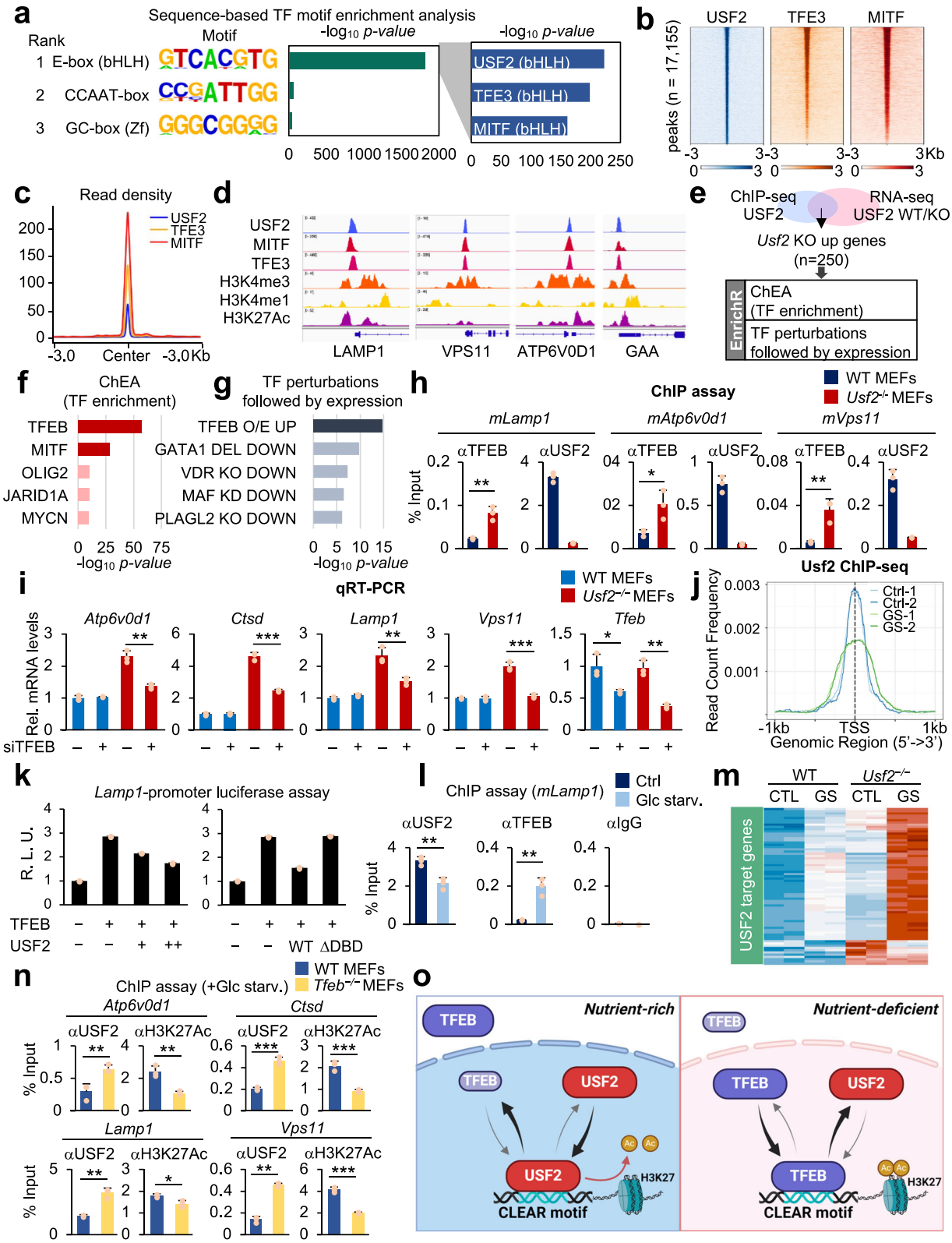

Enhancing lysosomal activity and autophagy by activating TFEB has emerged as a promising strategy for treating diseases caused by protein aggregation, including Alzheimer's disease with amyloid β aggregation and liver disease with ATZ aggregation[45]. Here, USF2 downregulation increased autophagy and lysosomal biogenesis. Furthermore, USF2 downregulation effectively enhanced the clearance of pathological aggregates, including ATZ. We believe that this strategy could be extended to other cellular aggregation-related diseases, including neurodegenerative diseases, thus highlighting USF2 as a potential therapeutic target for such conditions. These findings suggest that downregulating USF2 and/or inhibiting the interaction between USF2 and HDAC1 may enhance lysosomal biogenesis and functionality. TFEB activation and USF2 inhibition may act synergistically in treating advanced disease. These findings may help in developing methods for controlling protein-aggregation-related diseases.

Fig. 5 | USF2 and TFEB antagonistically regulate lysosomal genes. a In silico motif analysis using USF2 ChIP-seq data. **b** Heatmap depicting the enrichment of TFE3 and MITF at USF2 binding sites. Each row indicates a 6 kb window centered on a USF2 binding site. **c** Read density plots for ChIP-seq peaks of USF2, TFE3, and MITF. **d** Visualization of ChIP-seq peaks for USF2, MITF, TFE3, and histone modification markers H3K4me3, H3K4me1, H3K27Ac in USF2 target genes. **e** EnrichR gene set analysis of USF2 repressive target genes. **f** ChEA TF enrichment using *Usf2* KO up-regulated genes. **g** TF perturbation analysis using *Usf2* KO up-regulated genes. **h** ChIP assays on USF2-dependent promoters in WT and *Usf2*$^{-/-}$ MEFs using anti-TFEB and anti-USF2 antibodies. $n = 3$ technical replicates. Statistics by two-tailed *t*-test using WT and *Usf2*$^{-/-}$ MEFs as a comparison. **i** qRT-PCR assay of USF2 target genes in WT and *Usf2*$^{-/-}$ MEFs with or without TFEB knockdown. $n = 3$ technical replicates. Statistics by two-tailed *t*-test using WT and *Usf2*$^{-/-}$ MEFs as a comparison. **j** Normalized USF2 ChIP-seq peaks under normal and glucose starvation (GS) conditions. **k** *Lamp1* promoter-luciferase reporter assays. $n = 3$ technical replicates. **l** ChIP assays on the *Lamp1* promoter in WT MEFs under normal and GS conditions using anti-USF2 and anti-TFEB antibodies. $n = 3$ technical replicates. Statistics by two-tailed *t*-test using nutrient rich and glucose starved WT MEFs as comparison. **m** A heatmap illustrating expression of DEGs obtained from the RNA-seq results in WT and *Usf2*$^{-/-}$ MEFs under normal and GS conditions. **n** ChIP assays on USF2-dependent promoters in WT and *Tfeb*$^{-/-}$ MEFs under normal and GS conditions. $n = 3$ technical replicates. Statistics by two-tailed *t*-test using WT and *Tfeb*$^{-/-}$ MEFs as a comparison. **o** Schematics of the repression mechanism of USF2-NuRD complex. Data are presented as mean ± SEM. *, $p < 0.05$; **, $p < 0.01$; ***, $p < 0.001$. Figure 5/panel **o** Created with BioRender.com released under a Creative Commons Attribution-NonCommercial-NoDerivs 4.0 International license. Source data are provided as a Source Data file.

Our findings suggest potential drug targets in lysosome- and autophagy-related diseases, elucidate a transcriptional repression mechanism for the USF2–HDAC1–H3K27Ac axis and offer opportunities for the development of therapeutic approaches targeting this signaling axis.

Methods

Biological samples and the ethical use of animals

All animal experiments were conducted under protocols approved by the Institutional Animal Care and Use Committee (IACUC) of Seoul National University (SNU-200901-5-3), and all experimental procedures were performed in accordance with the Guidelines for the Care and Use of Laboratory Animals at the Institutional Animal Care and Use Committee (IACUC) of Seoul National University.

Antibodies and reagents

The following commercially available antibodies were used; anti-USF2 (ab125184, Abcam), anti-TFEB (ab2636, Abcam), anti-HDAC1 (C15410325-50, Diagenode), anti-CTSD (sc-377299, Santa Cruz), anti-ATP6V0D1 (ab202897, Abcam), anti-VPS11 (ab125083, Abcam), anti-Lamp1 (ab24170, Abcam), anti-LC3 (ab48394, ab51520, Abcam), anti-SQSTM1/p62 (ab101266, Abcam), anti-H3K27Ac (ab4729, Abcam), anti-GSK3β (sc-81462, Santa Cruz), anti-Phospho-GSK3β (Ser9) (9323, Cell Signaling Technology) and anti-β-actin (A1978, Sigma-Aldrich). The following chemicals were used in this study; Bafilomycin A1 (11038, Sigma), Lysosensor (L7535, Thermo Fisher Scientific), Lysotracker Green (L7526, Thermo Fisher Scientific), Lysotracker Red (L7528, Thermo Fisher Scientific) and DQ Red BSA (D12051, Thermo Fisher Scientific).

Cell culture and generation of shRNA knockdown cells

WT HepG2, shUSF2 HepG2, WT MEFs, *Usf2*$^{-/-}$ MEFs, and HeLa cells were cultured at 37 °C in Dulbecco's modified Eagle's medium (DMEM) containing 10 % fetal bovine serum (FBS) and antibiotics in a humidified incubator with 5 % CO_2. All cell lines were tested for mycoplasma contamination. For glucose starvation, cells were washed with DPBS and incubated with glucose-free DMEM supplemented with 10 % dialyzed FBS. Transfection was performed using Lipofectamine 3000 (L3000075, Invitrogen) according to the manufacturer's protocol. To generate USF2 knockdown cells, lentiviral shRNA constructs were first transfected along with viral packaging plasmids (psPAX2 and pMD2.G) into HEK293T cells. Three days after transfection, viral supernatant was filtered through 0.45 μ m filter and infected into targeting cells. Infected cells were then selected with 5 μg/ml puromycin. The targeting sequences of shRNAs are as follows.

hUSF2-1; 5′-TCCAGACTGTAACGCAGACAA-3′,
hUSF2-2; 5′-CGGCGACCACAACATCCAGTA-3′.

Generation of *Usf2*$^{-/-}$ mice and MEFs

Usf2 mutant mice were generated by introducing the gRNA/Cas9 RNP solution into fertilized eggs from the mating of B6D2F1 mice, as previously described[46]. The gRNA sequences used were 5′-GAGCCGCTTGCGCTGATCAC-3′ and 5′-GCTCTTCTTCTCTCATCTCG-3′. By mating the resulting *Usf2*$^{+/-}$ mice (founder generation) with wild-type mice, we established *Usf2* mutant mice with a 2112 bp deletion in the *Usf2* gene. Frozen spermatozoa from B6D2-*Usf2*, RBRC#11002, and CARD#2909 will be available through RIKEN BRC (http://en.brc.riken.jp/index.shtml) and CARD R-BASE (https://cardmice.com/rbase/). All animal experiments were conducted under protocols approved by the Institutional Animal Care and Use Committee (IACUC) of Seoul National University (SNU-200901-5-3).

WT and *Usf2*$^{-/-}$ MEFs were generated by crossing two *Usf2*$^{+/-}$ mice. The pregnant female *Usf2*$^{+/-}$ mice were euthanized at 13.5 days post-coitum (dpc). The embryos were dissected by removing their heads, limbs, gonads, tail, and other visceral masses. The embryos were then chopped and digested with 0.25 % trypsin/ethylenediaminetetraacetic acid (EDTA). The enzymatic activity was neutralized by adding DMEM with 10 % FBS and antibiotics. The tissues were pipetted up and down to obtain a single-cell suspension. The cells were cultured in 100 mm culture dishes until 70–80 % confluency and sub-cultured at a ratio of 1:4. MEFs were used at different passages (P1–10).

Preparation of whole-cell lysates

All cells were briefly rinsed with cold PBS before harvesting. For whole-cell lysates, the cells were resuspended in RIPA buffer (150 mM NaCl, 1 % Triton X-100, 1 % sodium deoxycholate, 0.1 % SDS, 50 mM Tris-HCl [pH 7.5], and 2 mM EDTA) supplemented with protease inhibitors and sonicated using a Branson Sonifier 450 at output 3 and a duty cycle of 30 for five pulses. For the cytosolic and nuclear fractions, cells were lysed in harvest buffer (10 mM HEPES [pH 7.9], 50 mM NaCl, 0.5 M sucrose, 0.1 mM EDTA, 0.5 % Triton X-100, DTT, PMSF, and protease inhibitors), incubated on ice for 5 min, and centrifuged at 120 × *g* for 10 min at 4 °C. The supernatant (cytosolic fraction) was transferred into a separate tube. The nuclear pellet was rinsed twice with 500 μl of buffer A (10 mM HEPES [pH 7.9], 10 mM KCl, 0.1 mM EDTA, and 0.1 mM EGTA) and centrifuged at 120 × *g* for 10 min at 4 °C. The supernatant was discarded, and the pellet (nuclear fraction) was resuspended in RIPA buffer and sonicated. All lysates were quantified using the Bradford method and analyzed by SDS–PAGE.

Immunofluorescence analysis

Immunocytochemistry was performed as described previously[12]. Cells grown on coverslips at a density of 3×10^4 cells/well in a 12-well plate were washed with PBS and fixed with 2 % formaldehyde in PBS for 10 min at room temperature. Fixed cells were permeabilized with 0.5 % Triton X-100 in PBS (PBS-T) and blocking step was performed with 3 % bovine serum albumin (BSA) in PBS-T for 1 h. Cells were incubated with antibodies overnight at 4 °C, followed by incubation with fluorescently labeled secondary antibodies for 1 h (Invitrogen), and mounted and visualized under a confocal microscope (Zeiss, LSM700). For

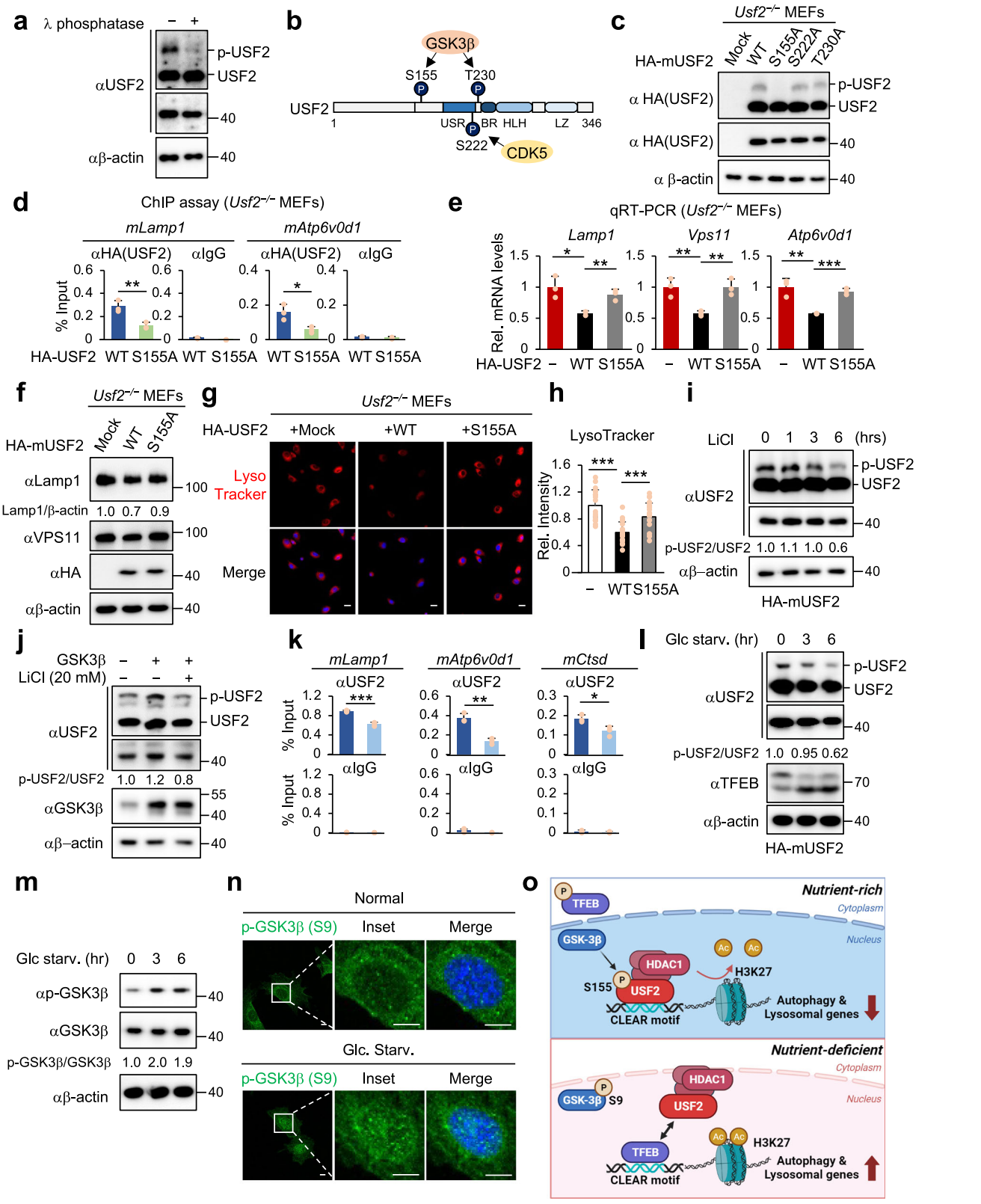

autophagy studies, MEFs were cultured in complete medium or glucose-starved medium for 24 h.

Lysotracker and Lysosensor assays

Cells were stained with 500 nM Lysotracker Green (L7526, Thermo Fisher Scientific), Lysotracker Red (L7528, Thermo Fisher Scientific) or Lysosensor (L7535, Thermo Fisher Scientific) for 4 h (25 °C, 5 % CO_2). After washing with the probe-free medium, the samples were observed using a confocal microscope (Zeiss, LSM 700).

DQ red BSA assay

Proteolytic activity of lysosomes in the cells was measured using DQ Red BSA (D12051, Thermo Fisher Scientific). The cells were plated at a density of 10,000 cells/well in 60 mm confocal dishes. The medium

Fig. 6 | Phosphorylation of USF2 at S155 by GSK3β enhances DNA-binding activity. a Immunoblot analysis in the presence or absence of λ-phosphatase treatment in WT MEFs. **b** Schematic representation of well-characterized phosphorylation sites on USF2 and the associated kinases responsible for this modification. **c** Immunoblot analysis using phos-tag™ gel conducted after reconstituting WT, S155A, S222A, and T230A mutants in *Usf2*$^{-/-}$ MEFs. **d** ChIP assay on the promoters of lysosomal genes following the reconstitution of WT and S155A mutant in *Usf2*$^{-/-}$ MEFs. $n = 3$ technical replicates. Statistics by two-tailed *t*-test using USF2 WT and S155A mutant expressed *Usf2*$^{-/-}$ MEFs as comparison. **e** qRT-PCR assay of lysosomal genes conducted after reconstituting mock, WT, and S155A mutant in *Usf2*$^{-/-}$ MEFs. $n = 3$ technical replicates. Statistical analysis performed using a two-tailed *t*-test. Mock and USF2 S155A mutant rescued cells were individually compared to USF2 WT rescued cells. **f** Immunoblot analysis of lysosomal proteins conducted after reconstituting mock, WT, and S155A mutant in *Usf2*$^{-/-}$ MEFs. **g** Representative images of Lysotracker staining. Lysotracker assay was performed after reconstituting mock, WT, and S155A mutant in *Usf2*$^{-/-}$ MEFs. Lysotracker, red; Hoechst, blue. Scale bar, 20 μm. **h** Quantification of Lysotracker intensity per cell. Lysotracker assay was performed after reconstituting mock, WT, and S155A mutant in *Usf2*$^{-/-}$ MEFs. $n = 18$ biologically independent samples. Statistical analysis performed using a two-tailed *t*-test. Mock and USF2 S155A mutant rescued cells were individually compared to USF2 WT rescued cells. **i** Immunoblot analysis using phos-tag™ gel under normal and LiCl treated conditions at different time points. **j** Immunoblot analysis using phos-tag™ gel under normal, GSK3β-overexpressed, and LiCl treated conditions. **k** ChIP assay on the promoters of lysosomal genes in WT MEFs under normal and LiCl treated condition. $n = 3$ technical replicates. Statistics by two-tailed *t*-test using normal and LiCl treated WT as comparison. **l** Immunoblot analysis using phos-tag™ gel for USF2 immunoblotting under normal and GS conditions. **m** Immunoblot analysis under normal and GS conditions in WT MEFs. **n** Representative confocal microscopic images using GSK3β Ser9 phosphorylation antibody under normal and GS conditions. p-GSK3β (Ser9), green; DAPI, blue. Scale bar, 10 μm. **o** Schematics of the regulation of autophagy and lysosome genes by USF2 and TFEB under nutrient-rich or deficient condition. Data are presented as mean ± SEM. *, $p < 0.05$; **, $p < 0.01$; ***, $p < 0.001$. Figure 6/panel **o** Created with BioRender.com released under a Creative Commons Attribution-NonCommercial-NoDerivs 4.0 International license. Source data are provided as a Source Data file.

was replaced with DMEM high glucose with 20 μg/ml DQ red BSA and incubated for 4 h (25 °C, 5 % CO_2). The fluorescent signal was measured using a confocal microscope (LSM 700, Zeiss).

Quantitative RT-PCR

Total RNA was extracted using Trizol (15596026, Invitrogen), and reverse transcription was performed from 1 μg of total RNA using an SRK-1000 SuPrimeScript cDNA Synthesis Kit (Genet Bio, Daejeon, Republic of Korea). The abundance of mRNAs was detected using an ABI prism 7500 system or BioRad CFX384 with SYBR TOPreal qPCR 2× PreMix (RT500, Enzynomics). The amount of mRNA was calculated using the ΔΔCt method, and *Hprt* was used as a control. All reactions were performed in triplicates. The following mouse primers were used in this study;

Ctsd; forward (fwd) 5′- TAAGACCACGGAGCCAGTGTCA-3′,
reverse (rev) 5′- CCACAGGTTAGAGGAGCCAGTA-3′;
Atp6v0d1; forward (fwd) 5′- GCATCTCAGAGCAGGACCTTGA-3′,
reverse (rev) 5′- GGATAGGACACATGGCATCAGC-3′;
Vps11; forward (fwd) 5′- ATCGGCAGTCTCTGGCTAATGC-3′,
reverse (rev) 5′- GGACCTTGATGGCTGTCTCTAC-3′;
Lamp1; forward (fwd) 5′- CCAGGCTTTCAAGGTGGACAGT-3′,
reverse (rev) 5′- GGTAGGCAATGAGGACGATGAG-3′;
Map1lc3b; forward (fwd) 5′- GTCCTGGACAAGACCAAGTTCC-3′,
reverse (rev) 5′- CCATTCACCAGGAGGAAGAAGG-3′;

ChIP and qRT–PCR analyzes

ChIP assays were performed as previously described[12]. Cells were cross-linked in 1 % formaldehyde for 10 min and washed with ice-cold PBS three times. After glycine quenching for 5 min, the cells were collected and lysed in a buffer containing 50 mM Tris–HCl (pH 8.1), 10 mM EDTA, and 1 % SDS, supplemented with a complete protease inhibitor cocktail (11873580001, Roche). After DNA fragmentation through sonication, chromatin extracts containing DNA fragments with an average of 250 bp were then diluted ten times with dilution buffer containing 1 % Triton X-100, 2 mM EDTA, 150 mM NaCl, and 20 mM Tris–HCl (pH 8.1) with complete protease inhibitor cocktail and subjected to immunoprecipitations overnight at 4 °C. Immunocomplexes were captured by incubating 40 μl of protein A/G Sepharose for 1.5 h at 4 °C. Beads were washed with TSE I buffer (0.1 % SDS, 1 % Triton X-100, 2 mM EDTA, 20 mM Tris–HCl (pH 8.1), and 150 mM NaCl), TSE II buffer (0.1 % SDS, 1 % Triton X-100, 2 mM EDTA, 20 mM Tris–HCl (pH 8.1), and 500 mM NaCl), buffer III (0.25 M LiCl, 1 % NP-40, 1 % deoxycholate, 10 mM Tris–HCl (pH 8.1), and 1 mM EDTA), three times TE buffer (10 mM Tris–HCl (pH 8.0) and 1 mM EDTA) and eluted in elution buffer (1 % SDS and 0.1 M $NaHCO_3$). The supernatant was incubated overnight at 65 °C to reverse crosslink and then digested with RNase A for 1 h at 37 °C and proteinase K for 2 h at 55 °C. ChIP and input DNA were then purified and analyzed for qRT–PCR analysis or used for constructing sequencing libraries.

The following primers were used;
Atp6v0d1; forward (fwd) 5′- CAACTAGACTCCCCGGATCA-3′,
reverse (rev) 5′- GTCGGGCACTCCAGAGTAA-3′;
Lamp1; forward (fwd) 5′- GTGGGGAGAGGGCAAGATA-3′,
reverse (rev) 5′- CGCCAGCTTACTCCTCACTT−3′;
Vps11; forward (fwd) 5′- TCCTTCACCAGCTCCTTCTC-3′,
reverse (rev) 5′- GAGCAGCAAGCCTTTTGTG-3′;
Ctsd; forward (fwd) 5′- CGGCTTATAGGCAGGATGAC-3′,
reverse (rev) 5′- GTGCGTAGGCCTGGAGTAGG-3′;

Transfection of siRNA

LipofectamineTM 3000 transfection reagent kit (Invitrogen, L3000001) was used according to the manufacturer's protocol to transfect siRNA targeting the gene to cells. Lipofectamine 3000-siRNA complex was initially generated in volume ratio of 2:1 and mixed and incubated for 15 min at room temperature. The mixture was then added onto cells in culture dish in confluency of 70–80% for 6 h in final siRNA concentration of 20 nM. The Lipofectamine complex was washed out after 6 h with fresh media and culture overnight. The following sequences of siRNA were used;

si*Tfeb*; 5′-GCAGGCTGTCATGCATTATAT-3′,
si*USF2*; 5′-TCCTCCACTTGGAAACGGTAT-3′.

Immunohistochemistry

WT and *Usf2*$^{-/-}$ embryos were fixed in 10 % formalin (HT5011, Sigma) overnight at 4 °C. Tissues were sequentially dehydrated in ethanol at concentrations ranging from 50 % to 100 %. Dehydrated specimens were subsequently infiltrated with 100 % xylene and embedded in paraffin wax. For immunostaining, tissues were sectioned at 7 μm thickness and blocked with 5 % BSA. Sections were then stained with the primary antibodies for 4 h at 25 °C. For the secondary reaction, Alexa Fluor 488-labeled secondary antibodies were used, and sections were mounted with DAPI (D9542, Sigma). The mounted sections were visualized under a confocal microscope (LSM700, Zeiss).

Hematoxylin and eosin (H&E) staining

Hematoxylin and eosin (H&E) staining was performed as described previously[47]. In brief, mouse liver samples are collected, washed three times with PBS to remove blood. Fix the samples in 4 % formaldehyde solution for 20 h at 4 °C. They are then dehydrated with ethanol, embedded in paraffin, and cut into slides. After the slides are deparaffinized and rehydrated in an oven, they are stained with hematoxylin. After the staining process, rinse 3 times with quick soaking in 0.3 % acid

https://doi.org/10.1038/s41467-024-52600-2

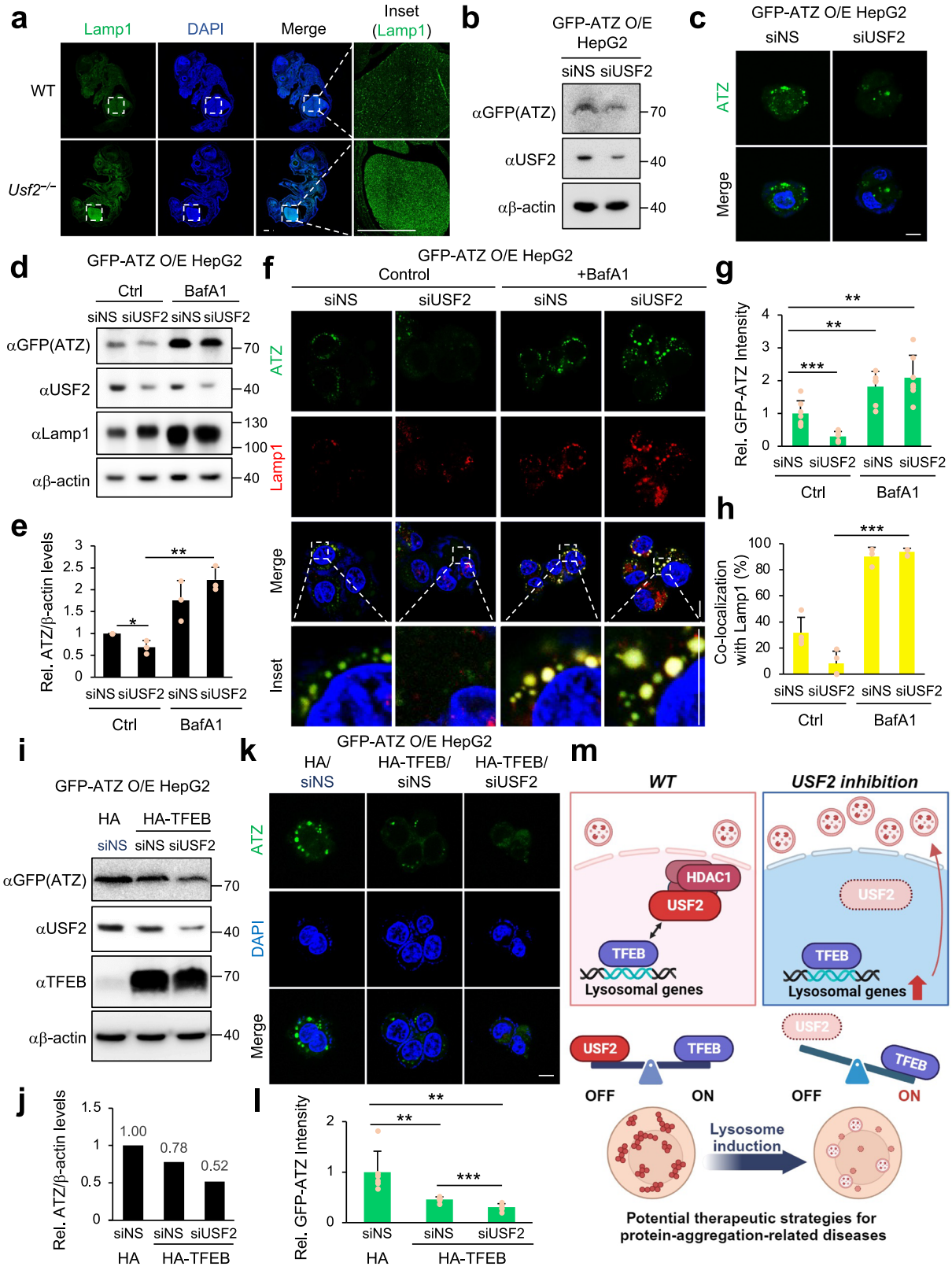

alcohol. After counterstaining with eosin, wash with ethanol and xylene and cover slip. Liver tissue is analyzed under a light microscope.

RNA-seq analysis

RNA-seq libraries were prepared using the TruSeq Stranded mRNA LT Sample Prep Kit (Illumina) according to the manufacturer's instructions. RNAseq libraries were paired-end sequenced on an Illumina HiSeq 4000 (Macrogen). RNA-seq data were mapped using STAR (v2.7.10b) against the mouse genome (GRCm38). Read counts were generated by featureCounts (v2.0.3). The differential gene expression analysis was performed using Bioconductor package DESeq2 (v1.38.3). A clustering heatmap was drawn using a z-score that is scaled across samples for each gene. Functional enrichment analysis of GOBPs and KEGG pathways was performed using a clusterProfiler.

Fig. 7 | Inhibition of USF2 stimulates clearance of α1-Antitrypsin Mutant Z. **a** Immunofluorescence staining to detect the expression of lysosomal proteins, such as Lamp1, in 16.5-day-old WT and *Usf2*$^{-/-}$ embryos. Lamp1, green; Hoechst, blue. Scale bar, 1 mm. **b** Immunoblot analysis of GFP-ATZ following the transfection of siNS or siUSF2 into HepG2 cell lines stably expressing GFP-ATZ (GFP-ATZ O/E HepG2). **c** Representative confocal microscopic images of GFP-ATZ in cells as in **b**. Scale bar, 10 μm. **d** Immunoblot analysis of GFP-ATZ O/E HepG2 cell lines with and without USF2 knockdown and in the presence or absence of Bafilomycin A1 (BafA1) treatment. **e** Quantification of GFP-ATZ protein levels relative to β-actin. $n = 3$ biologically independent samples. Statistical analysis performed using a two-tailed *t*-test. siNS and siUSF2+BafA1 cells were individually compared to siUSF2 cells. **f** Representative confocal microscopic images of GFP-ATZ O/E HepG2 cell lines with and without USF2 knockdown and in the presence or absence of BafA1 treatment. ATZ, green; Lamp1, red; DAPI, blue. Scale bar, 10 μm. **g** Quantification of GFP-ATZ intensity. $n = 7$ biologically independent samples. Statistical analysis performed using a two-tailed *t*-test. siUSF2, siNS+BafA1 and siUSF2+BafA1 cells were individually compared to siNS cells. **h** Quantification of co-localization of Lamp1 and GFP-ATZ. $n = 3$ biologically independent samples. Statistical analysis performed using a two-tailed *t*-test. siUSF2 treated cells were compared to siUSF2+BafA1 treated cells. **i** Immunoblot analysis of GFP-ATZ O/E HepG2 cell lines after overexpression of TFEB and knockdown of USF2. **j** Quantification of GFP-ATZ protein levels relative to β-actin. **k** Representative confocal images of GFP-ATZ O/E HepG2 cell lines after overexpression of TFEB and knockdown of USF2. Scale bar, 10 μm. **l** Quantification of GFP-ATZ intensity. $n = 5$ biologically independent samples. Statistical analysis performed using a two-tailed *t*-test. siNS, siNS+HA-TFEB cells were individually compared to siUSF2+HA-TFEB cells. **m** Schematics of therapeutic strategies for α1-antitrypsin deficiency by enhancing autophagy and lysosomal function through the inhibition of USF2 and the activation of TFEB. Data are presented as mean ± SEM. **, $p < 0.01$; ***, $p < 0.001$. Figure 7/panel **m** Created with BioRender.com released under a Creative Commons Attribution-NonCommercial-NoDerivs 4.0 International license. Source data are provided as a Source Data file.

ChIP-seq analysis

ChIP-seq libraries were prepared for sequencing using the TruSeq DNA Sample Prep Kit, according to the manufacturer's instructions. ChIP-seq libraries were paired-end sequenced on an Illumina HiSeq 4000 (Macrogen). ChIP-seq reads were aligned to the mouse reference genome (GRCm38) using Bowtie2 (v2.5.1). Peaks were called using Macs2 (v2.2.7.1). BigWig files were generated using bamCoverage (v3.5.1). USF2 upon glucose starvation was compared against control input. We used anti-USF2 and anti-H3K27Ac antibodies for ChIP-seq.

ATAC-seq analysis

ATAC-seq libraries were prepared for sequencing using Illumina Tagment DNA TDE1 Enzyme and Buffer Kits (#20034197, Illumina) and paired-end sequencing was performed by Illumina HiSeq 4000 (Macrogen). ATAC-seq reads were aligned to the mouse reference genome (GRCm38) using Bowtie2 (v2.5.1). Peaks were called using Macs2 (v2.2.7.1). BigWig files were generated using bamCoverage (v3.5.1).

LC–MS/MS analysis

Transfected HEK293T cells were lysed with EBC200 buffer (50 mM Tris-HCl [pH 8.0], 200 mM NaCl, 0.5% NP-40, and protease inhibitor) and followed by centrifugation. Supernatant was incubated with GFP-Trap at 4 °C for 1 hr. The beads were washed with EBC200 buffer twice. The remaining supernatant is removed. The elutes were obtained with 100 ml acidic elution buffer (200 mM glycine [pH 2.5]) and neutralized by 10 μl neutralization buffer (1 M Tris [pH 10.4]). A Thermo Scientific Quadrupole-Orbitrap instrument (Thermo Scientific, USA) equipped with Dionex U 3000 RSLCnano HPLC system was used. Mass spectrometric analyzes were performed using a Thermo Scientific Orbitrap Exploris 240 mass spectrometer. Fractions were reconstituted in solvent A (Water/Acetonitrile (98:2 v/v), 0.1 % Formic acid) and then injected into LC-nano ESI-MS/MS system. Samples were first trapped on a Acclaim PepMap 100 trap column (100 μm × 2 cm, nanoViper C18, 5 μm, 100 Å, Thermo Scientific, part number 164564) and washed for 6 min with solvent A (water/ACN (98:2 v/v), 0.1 % Formic acid at a flow rate of 4 μL/min, and then separated on a PepMap RSLC C18 column (75 μm × 15 cm, nanoViper C18, 3 μm, 100 Å, Thermo Scientific, part number ES900) at a flow rate of 300 nL/min. The LC gradient was run at 2% to 8% solvent B over 10 min, then from 8% to 30% over 55 min, followed by 90% solvent B (100% ACN and 0.1% Formic acid) for 4 min, and finally 2% solvent B for 20 min. Xcaliber software version 4.4 was used to collect MS data. The Orbitrap analyzer scanned precursor ions with a mass range of 350–1800 m/z with 60,000 resolution at m/z 200. Mass data are acquired automatically using proteome discoverer 2.5 (Thermo Scientific, USA). $n = 1$ for technical replicates.

Statistical analysis

Experiments were performed independently at least three times. Random images were chosen for Lysotracker and DQ red BSA intensity counting. Lysotracker and DQ red BSA staining intensity was measured using ImageJ. *P* values were calculated using one-tailed *t*-tests. For animal studies, sample size was determined empirically based on previous studies to ensure appropriate statistical power. Mice were randomly chosen for fasting. No animals were excluded from statistical analysis, and the investigators were not blinded to the study. Values are expressed as mean ± SD. Significance was analyzed using a two-tailed, unpaired *t*-test. Statistical significance was set at $p < 0.05$.

Reporting summary

Further information on research design is available in the Nature Portfolio Reporting Summary linked to this article.

Data availability

Raw ATAC-seq, ChIP-seq, and RNA-seq data have been deposited in the Gene Expression Omnibus (GEO) under accession code GSE252309, GSE252310, GSE252311, respectively. We downloaded the call sets from the ENCODE portal (https://www.encodeproject.org/) with the following identifiers: (mouse) USF2(ENCSR000ETW, ENCSR000ETF, and ENCSR000ERJ), H3K4me3(ENCSR000CGK), H3K4me1(ENCSR000DHQ), H3K27Ac(ENCSR000CGJ), H3K9Ac(ENCSR000CGL), H3K27me3(ENCSR000DHY), H3K9me3(ENCSR000DHO), (human) USF2(ENCSR578KEN), HDAC1(ENCSR362CPB), HDAC2(ENCSR337NWW), CHD4(ENCSR431FOF), GATAD2A(ENCSR925BFV), GATAD2B(ENCSR250LJG), MTA1(ENCSR983KRB), MITF(ENCSR797SWM), and TFE3(ENCSR953KEY). The mass spectrometry raw data have been deposited in a ProteomeXchange partner repository, PRIDE under accession code PXD050434. Source data are provided with this paper.

Code availability

The custom codes are deposited in a public DOI-minting repository: https://github.com/YoungS-Yu/TFenrichment_Yu (https://doi.org/10.5281/zenodo.13251138).

References

1. Klionsky, D. J. & Emr, S. D. Autophagy as a regulated pathway of cellular degradation. *Science* **290**, 1717–1721 (2000).
2. Mizushima, N., Levine, B., Cuervo, A. M. & Klionsky, D. J. Autophagy fights disease through cellular self-digestion. *nature* **451**, 1069–1075 (2008).
3. Ballabio, A. & Bonifacino, J. S. Lysosomes as dynamic regulators of cell and organismal homeostasis. *Nat. Rev. Mol. cell Biol.* **21**, 101–118 (2020).

4. Parenti, G., Andria, G. & Ballabio, A. Lysosomal storage diseases: from pathophysiology to therapy. *Annu. Rev. Med.* **66**, 471–486 (2015).
5. Platt, F. M., d'Azzo, A., Davidson, B. L., Neufeld, E. F. & Tifft, C. J. Lysosomal storage diseases. *Nat. Rev. Dis. Prim.* **4**, 27 (2018).
6. Settembre, C. et al. TFEB links autophagy to lysosomal biogenesis. *science* **332**, 1429–1433 (2011).
7. Sardiello, M. et al. A gene network regulating lysosomal biogenesis and function. *Science* **325**, 473–477 (2009).
8. Zhou, J. et al. FOXO3 induces FOXO1-dependent autophagy by activating the AKT1 signaling pathway. *Autophagy* **8**, 1712–1723 (2012).
9. Mammucari, C. et al. FoxO3 controls autophagy in skeletal muscle in vivo. *Cell Metab.* **6**, 458–471 (2007).
10. Annunziata, I. et al. MYC competes with MiT/TFE in regulating lysosomal biogenesis and autophagy through an epigenetic rheostat. *Nat. Commun.* **10**, 3623 (2019).
11. Yu, Y. S., Kim, H., Kim, K. I. & Baek, S. H. Epigenetic regulation of autophagy by histone-modifying enzymes under nutrient stress. *Cell Death Differ.* **30**, 1430–1436 (2023).
12. Shin, H.-J. R. et al. AMPK–SKP2–CARM1 signalling cascade in transcriptional regulation of autophagy. *Nature* **534**, 553–557 (2016).
13. Yu, Y. S. et al. Pontin arginine methylation by CARM1 is crucial for epigenetic regulation of autophagy. *Nat. Commun.* **11**, 6297 (2020).
14. Füllgrabe, J. et al. The histone H4 lysine 16 acetyltransferase hMOF regulates the outcome of autophagy. *Nature* **500**, 468–471 (2013).
15. Corre, S. & Galibert, M. D. Upstream stimulating factors: highly versatile stress-responsive transcription factors. *Pigment cell Res.* **18**, 337–348 (2005).
16. Cogswell, J. P., Godlevski, M. M., Bonham, M., Bisi, J. & Babiss, L. Upstream stimulatory factor regulates expression of the cell cycle-dependent cyclin B1 gene promoter. *Mol. Cell. Biol.* **15**, 2782–2790 (1995).
17. Chang, L. A., Smith, T., Pognonec, P., Roeder, R. G. & Murialdo, H. Identification of USF as the ubiquitous murine factor that binds to and stimulates transcription from the immunoglobulin λ2 chain promoter. *Nucleic acids Res.* **20**, 287–293 (1992).
18. Casado, M., Vallet, V. S., Kahn, A. & Vaulont, S. Essential role in vivo of upstream stimulatory factors for a normal dietary response of the fatty acid synthase gene in the liver. *J. Biol. Chem.* **274**, 2009–2013 (1999).
19. Wang, D. & Sul, H. S. Upstream stimulatory factors bind to insulin response sequence of the fatty acid synthase promoter USF1 is regulated. *J. Biol. Chem.* **270**, 28716–28722 (1995).
20. Galibert, M.-D., Carreira, S. & Goding, C. R. The Usf-1 transcription factor is a novel target for the stress-responsive p38 kinase and mediates UV-induced Tyrosinase expression. *EMBO J.* **20**, 5022–5031 (2001).
21. Corre, S. et al. UV-induced expression of key component of the tanning process, the POMC and MC1R genes, is dependent on the p-38-activated upstream stimulating factor-1 (USF-1). *J. Biol. Chem.* **279**, 51226–51233 (2004).
22. Pajukanta, P. et al. Familial combined hyperlipidemia is associated with upstream transcription factor 1 (USF1). *Nat. Genet.* **36**, 371–376 (2004).
23. Nicolas, G. et al. Lack of hepcidin gene expression and severe tissue iron overload in upstream stimulatory factor 2 (USF2) knockout mice. *Proc. Natl Acad. Sci.* **98**, 8780–8785 (2001).
24. Sirito, M., Lin, Q., Deng, J. M., Behringer, R. R. & Sawadogo, M. Overlapping roles and asymmetrical cross-regulation of the USF proteins in mice. *Proc. Natl Acad. Sci.* **95**, 3758–3763 (1998).
25. Gao, E., Wang, Y., Alcorn, J. L. & Mendelson, C. R. Transcription factor USF2 is developmentally regulated in fetal lung and acts together with USF1 to induce SP-A gene expression. *Am. J. Physiol.-Lung Cell. Mol. Physiol.* **284**, L1027–L1036 (2003).
26. Palmieri, M. et al. Characterization of the CLEAR network reveals an integrated control of cellular clearance pathways. *Hum. Mol. Genet.* **20**, 3852–3866 (2011).
27. Napolitano, G. et al. mTOR-dependent phosphorylation controls TFEB nuclear export. *Nat. Commun.* **9**, 3312 (2018).
28. Horbach, T. et al. GSK3β-dependent phosphorylation alters DNA binding, transactivity and half-life of the transcription factor USF2. *PLoS One* **9**, e107914 (2014).
29. Sayasith, K., Lussier, J. G. & Sirois, J. Role of upstream stimulatory factor phosphorylation in the regulation of the prostaglandin G/H synthase-2 promoter in granulosa cells. *J. Biol. Chem.* **280**, 28885–28893 (2005).
30. Chi, T. F., Horbach, T., Götz, C., Kietzmann, T. & Dimova, E. Y. Cyclin-dependent kinase 5 (CDK5)-mediated phosphorylation of upstream stimulatory factor 2 (USF2) contributes to carcinogenesis. *Cancers* **11**, 523 (2019).
31. Stambolic, V. & Woodgett, J. R. Mitogen inactivation of glycogen synthase kinase-3 β in intact cells via serine 9 phosphorylation. *Biochemical J.* **303**, 701–704 (1994).
32. Jope, R. S. & Johnson, G. V. The glamour and gloom of glycogen synthase kinase-3. *Trends biochemical Sci.* **29**, 95–102 (2004).
33. Kamimoto, T. et al. Intracellular inclusions containing mutant α1-antitrypsin Z are propagated in the absence of autophagic activity. *J. Biol. Chem.* **281**, 4467–4476 (2006).
34. Tzakis, A. Early recognition of alpha-1 antitrypsin deficiency and considerations for liver transplantation. *Gastroenterol. Hepatol.* **9**, 110 (2013).
35. Cummings, E. E. et al. Deficient and null variants of SERPINA1 are proteotoxic in a Caenorhabditis elegans model of α1-antitrypsin deficiency. *PLoS One* **10**, e0141542 (2015).
36. Hidvegi, T. et al. An autophagy-enhancing drug promotes degradation of mutant α1-antitrypsin Z and reduces hepatic fibrosis. *Science* **329**, 229–232 (2010).
37. Pastore, N. et al. Gene transfer of master autophagy regulator TFEB results in clearance of toxic protein and correction of hepatic disease in alpha-1-anti-trypsin deficiency. *EMBO Mol. Med.* **5**, 397–412 (2013).
38. Chi, T. F. et al. Loss of USF2 promotes proliferation, migration and mitophagy in a redox-dependent manner. *Redox Biol.* **37**, 101750 (2020).
39. Liu, C., Gao, Q., Dong, J. & Cai, H. Usf2 deficiency promotes autophagy to alleviate cerebral ischemia-reperfusion injury through suppressing YTHDF1-m6A-Mediated Cdc25A Translation. *Mol. Neurobiol.* **61**, 2556–2568 (2024).
40. Zhou, L. et al. Syntaxin-6 promotes the progression of hepatocellular carcinoma and alters its sensitivity to chemotherapies by activating the USF2/LC3B axis. *Int. J. Biol. Sci.* **19**, 3892 (2023).
41. Chen, B. et al. USF2 promotes autophagy and proliferation in chronic lymphocytic leukemia by inhibiting STUB1-induced NFAT5 ubiquitination. *Ann. Hematol.* **103**, 533–544 (2024).
42. Settembre, C. et al. A lysosome-to-nucleus signalling mechanism senses and regulates the lysosome via mTOR and TFEB. *EMBO J.* **31**, 1095–1108 (2012).
43. Martina, J. A. et al. The nutrient-responsive transcription factor TFE3 promotes autophagy, lysosomal biogenesis, and clearance of cellular debris. *Sci. Signal.* **7**, ra9 (2014).
44. Li, L. et al. A TFEB nuclear export signal integrates amino acid supply and glucose availability. *Nat. Commun.* **9**, 2685 (2018).
45. Zhang, Y.-d & Zhao, J.-j TFEB participates in the Aβ-induced pathogenesis of Alzheimer's disease by regulating the autophagy-lysosome pathway. *DNA cell Biol.* **34**, 661–668 (2015).
46. Noda, T. et al. Nine genes abundantly expressed in the epididymis are not essential for male fecundity in mice. *Andrology* **7**, 644–653 (2019).
47. Kim, D. et al. PKCα-LSD1-NF-κB-signaling cascade is crucial for epigenetic control of the inflammatory response. *Mol. cell* **69**, 398–411.e396 (2018).

Acknowledgements
This work was supported by grants from the Creative Research Initiatives Program (Research Center for Epigenetic Code and Diseases) [2017R1A3B1023387 to S.H.B.]; Science Research Center Program (Cellular Heterogeneity Research Center) [NRF-RS-2023-00207857 to K.I.K.]; Basic Science Research Program [NRF-2021R1A2C1006680 to K.I.K.]; Sejong Science Fellowship Program [NRF-2021R1C1C2010332 to Y.S.Y.] from the National Research Foundation (NRF) grant funded by the Korea government. We acknowledge the support of the following funding agencies: the Italian Telethon Foundation; Fondazione AIRC per la ricerca sul cancro (5 × 1000-21051 to A.B.); and the European Research Council H2020 AdG (LYSOSOMICS 694282). Figures in this paper were created using BioRender.com.

Author contributions
J.K., Y.S.Y., Y.C., D.-H.L., D.K., H.K., A.B., K.I.K., and S.H.B. conceptualized this work; J.K., Y.S.Y., Y.C., D.-H.L., S.H., and J.-h.K. performed the cell biology and biochemistry experiments; J.K. and Y.S.Y. prepared and analyzed RNA-seq, ChIP-seq, and ATAC-seq; T.N. and M.I. generated and bred the *Usf2* heterozygote mice; J.K. and Y.C. performed the *Usf2*$^{-/-}$ mice lethality tests and embryonic studies; J.K., Y.S.Y., K.I.K., and S.H.B. organized and analyzed the data; J.K., Y.S.Y., K.I.K., and S.H.B. wrote the manuscript.

Competing interests
A.B. is cofounder of CASMA Therapeutics, Inc., and Advisory board member of NexGeneration Diagnostics and Avilar Therapeutics. The remaining authors declare no competing interests.

Additional information
Supplementary information The online version contains supplementary material available at https://doi.org/10.1038/s41467-024-52600-2.

Correspondence and requests for materials should be addressed to Keun Il Kim or Sung Hee Baek.

Peer review information *Nature Communications* thanks Masaaki Komatsu and the other, anonymous, reviewer(s) for their contribution to the peer review of this work. A peer review file is available.

[1]Creative Research Initiatives Center for Epigenetic Code and Diseases, School of Biological Sciences, Seoul National University, Seoul, South Korea. [2]Department of Biological Sciences, Sookmyung Women's University, Seoul, Republic of Korea. [3]Research Institute for Microbial Diseases, Osaka University, Osaka, Japan. [4]Institute of Resource Development and Analysis, Kumamoto University, Kumamoto, Japan. [5]Priority Organization for Innovation and Excellence, Kumamoto University, Kumamoto, Japan. [6]The Institute of Medical Science, The University of Tokyo, Tokyo, Japan. [7]Department of Anatomy, College of Medicine, The Catholic University of Korea, Seoul, Republic of Korea. [8]Department of Biochemistry and Molecular Biology, Korea University College of Medicine, Seoul, Republic of Korea. [9]BK21 Graduate Program, Department of Biomedical Sciences, Korea University College of Medicine, Seoul, Republic of Korea. [10]Telethon Institute of Genetics and Medicine (TIGEM), Naples, Italy. [11]Medical Genetics Unit, Department of Medical and Translational Science, Federico II University, Naples, Italy. [12]Department of Molecular and Human Genetics, Baylor College of Medicine, Houston, TX, USA. [13]Jan and Dan Duncan Neurological Research Institute, Texas Children's Hospital, Houston, TX, USA. [14]These authors contributed equally: Jaebeom Kim, Young Suk Yu.
✉e-mail: kikim@sookmyung.ac.kr; sbaek@snu.ac.kr